Continued Investigations of Respirable Release Fractions for Stress Corrosion Crack-Like Geometries

Spent Fuel and Waste Disposition

Prepared for
US Department of Energy
Spent Fuel and Waste Science and Technology

S. Durbin, R. Pulido, A. Perales, E. Lindgren,
P. Jones, H. Mendoza, and J. Phillips
Sandia National Laboratories

M. Lanza, and A. Casella
Pacific Northwest National Laboratory

July 29, 2021
Milestone No. M2SF-21SN010207071
SAND2021-9222 R

Prepared by
Sandia National Laboratories
Albuquerque, New Mexico 87185 and Livermore, California 94550

Sandia National Laboratories is a multimission laboratory managed and operated by National Technology and Engineering Solutions of Sandia, LLC, a wholly owned subsidiary of Honeywell International, Inc., for the U.S. Department of Energy's National Nuclear Security Administration under contract DE-NA0003525.

ABSTRACT

The formation of a stress corrosion crack (SCC) in the canister wall of a dry cask storage system (DCSS) has been identified as a potential issue for the long-term storage of spent nuclear fuel. The presence of an SCC in a storage system could represent a through-wall flow path from the canister interior to the environment. Modern, vertical DCSSs are of particular interest due to the commercial practice of using relatively high backfill pressures (up to approximately 800 kPa) in the canister to enhance internal natural convection. This pressure differential offers a comparatively high driving potential for blowdown of any particulates that might be present in the canister. In this study, the rates of gas flow and aerosol transmission of a spent fuel surrogate through an engineered microchannel with dimensions representative of an SCC were evaluated experimentally using coupled mass flow and aerosol analyzers. The microchannel was formed by mating two gage blocks with a linearly tapering slot orifice nominally 13 μm (0.005 in.) tall on the upstream side and 25 μm (0.0010 in.) tall on the downstream side. The orifice is 12.7 mm (0.500 in.) wide by 8.89 mm (0.350 in.) long (flow length). Surrogate aerosols of cerium oxide, CeO_2, were seeded and mixed with either helium or air inside a pressurized tank. The aerosol characteristics were measured immediately upstream and downstream of the simulated SCC at elevated and ambient pressures, respectively. These data sets are intended to demonstrate a new capability to characterize SCCs under well-controlled boundary conditions. Modeling efforts were also initiated that evaluate the depletion of aerosols in a commercial dry storage canister. These preliminary modeling and ongoing testing efforts are focused on understanding the evolution in both size and quantity of a hypothetical release of aerosolized spent fuel particles from failed fuel to the canister interior and ultimately through an SCC.

This page is intentionally left blank.

ACKNOWLEDGEMENTS

This work was funded by the U.S. Department of Energy (DOE), Office of Nuclear Energy Spent Fuel and Waste Disposition Research and Development Program.

The technologist team of Greg Koenig, Thad Vice, Ron Williams, and Beau Baigas are commended for their tireless efforts and attention to detail in making this work possible. The authors would like to express their appreciation to Ned Larson of the DOE for his programmatic leadership and vision. Parallel modeling efforts by Yadu Sasikumar at Oak Ridge National Laboratory of these tests are eagerly anticipated.

This page is intentionally left blank.

CONTENTS

LIST OF FIGURES

LIST OF TABLES

This page is intentionally left blank.

ACRONYMS

AED	aerodynamic equivalent diameter
alpm	actual liters per minute
DCSS	dry cask storage system
DOE	US Department of Energy
EDM	electrical discharge machining
GSD	geometric standard deviation
HEPA	high-efficiency particulate absorbing
MMD	mass median diameter
NE	nuclear energy
ORNL	Oak Ridge National Laboratory
PNNL	Pacific Northwest National Laboratory
RBG	rotating brush generator
SCC	stress corrosion crack
SFWD	Spent Fuel and Waste Disposition
slpm	standard liters per minute
SNF	spent nuclear fuel
SNL	Sandia National Laboratories
STP	standard temperature and pressure

This page is intentionally left blank.

CONTINUED INVESTIGATIONS OF RESPIRABLE RELEASE FRACTIONS FOR STRESS CORROSION CRACK-LIKE GEOMETRIES

This report fulfills milestone M2SF-21SN010207071 in the Aerosol Source Term work package (SF-21SN01020707). This work was sponsored under the Department of Energy's (DOE) Office of Nuclear Energy (NE) Spent Fuel and Waste Disposition (SFWD) campaign.

1 INTRODUCTION

Dry cask storage systems (DCSSs) for spent nuclear fuel (SNF) are designed to provide a confinement barrier that prevents the release of radioactive material, maintains SNF in an inert environment, provides radiation shielding, and maintains subcriticality conditions. SNF is initially stored in pools of water for cooling where the water also provides radiation shielding. As these pools get closer to capacity, dry storage systems are becoming the primary means of extended storage. After sufficient cooling in pools, SNF is loaded into a canister and placed inside a storage cask, where the canister is welded shut. The DCSS is then decontaminated and dried, and the system is moved to an on-site dry storage location. Figure 1.1 shows the major components of a DCSS for SNF.

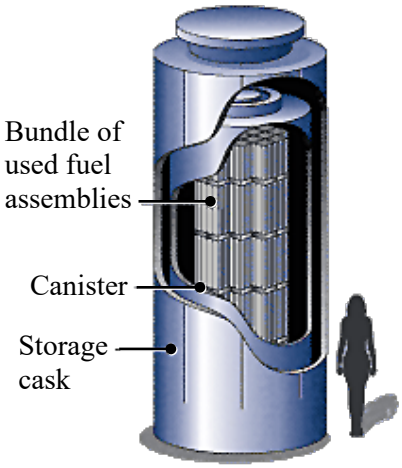

Source: https://www.nrc.gov/waste/spent-fuel-storage/diagram-typical-dry-cask-system.html

Figure 1.1 Typical dry cask storage system.

Typically, the canisters are made of stainless steel. The dry storage system is designed with an open volume between the canister and the storage cask. Rejection of the decay heat is accomplished by air flowing from air inlets at the bottom of the cask to outlets at the top via natural convection. This passively cooled design also allows dust from the environment into the system. These particulates may then collect on the surfaces of the canister. As the SNF cools, salts contained in the dust may deliquesce in the presence of moisture from the ambient relative humidity to form concentrated brines, which may contain corrosive species such as chlorides. These species can cause localized corrosion, called pitting. With sufficient stresses, these pits can evolve into stress corrosion cracks (SCCs), which could penetrate through the canister wall and allow communication from the interior of the canister to the external environment [Schindelholz, 2017].

1.1 Objective

The purpose of this on-going research is to explore the characterization of aerosols in DCSSs that have developed a through-wall SCC. The characteristics of interest include particulate suspension, transport, depletion, and transfer/deposition in the SCC.

This testing employed engineered slots with characteristic dimensions similar to those in SCCs as analogs. A more advanced geometry was explored in this testing to better approximate SCCs.

A Palas Promo 3000 HP high resolution aerosol spectrometer has been integrated into the experimental system that can directly monitor aerosol samples at elevated pressures. This high-pressure aerosol characterization system is designed to opto-mechanically switch between monitoring upstream and downstream sensing detector elements offering nearly simultaneous real-time measurements and eliminating the instrument bias seen in previous testing [Durbin *et al.*, 2018]. This test apparatus has consistently demonstrated a flexible technological approach to directly measure aerosol transmission through the engineered microchannel/slot at conditions of interest.

1.2 Previous Studies

The data obtainable from the measurement of particulate segregation in flows through open channels has significance in multiple fields. Studies include particle penetration through building cracks [Lewis, 1995, Liu and Nazaroff, 2003, Mosley *et al.*, 2001] to nuclear reactor safety [Powers, 2009], and more recently, storage and transportation of SNF in dry casks. Studies of these systems contribute to the understanding of particulate segregation through small channels as functions of particle size and concentration, channel dimensions, and differential pressures.

Previous work has contributed to the characterization of particulate segregation across channel flow for a range of particle sizes in aerosols. Lewis [Lewis, 1995] was motivated by a lack of empirical studies to support the development of protection factors against solid particles for enclosures. This protection factor was taken as the ratio of the dose of an outside concentration of particulates to the dose accumulated inside an enclosure for a specified time, with the doses defined as concentration-time integrals. Models were derived describing the total transport fraction of particles across a rectangular slot into an enclosure as functions of particle size, differential pressures, and slot heights. Lewis described an experimental apparatus with synthesized aerosols (containing either talc, aluminum oxide, titanium oxide, various silica powders, or ambient dust) mixed in a chamber containing an enclosure with a rectangular slot open to the chamber. A differential pressure was established between the chamber and the enclosure. Protection factors were found by comparing mass concentration values inside and outside the enclosure over a given time. The primary observations here were the decrease in total transport fraction with increasing particle size from 1-10 μm as well as a decrease in protection factor (corresponding to an increase in total transport fraction) with increasing differential pressures and slot heights.

Liu and Nazaroff [Liu and Nazaroff, 2003] conducted experiments of aerosol flow through rectangular slots using various building materials, including aluminum, brick, concrete, and wood. The slot heights were 0.25 mm and 1 mm, which are large compared to the micron- to submicron-sized particles they flowed through the cracks. They obtained data for particle penetration (defined as the ratio of downstream to upstream particle concentration), related to total transport fraction, as a function of particle size. They found that, for 0.25 mm cracks, particle sizes between 0.1-1 μm achieved penetration factors near unity, while smaller and larger particles showed diminished penetration factors for pressure differentials of 4 and 10 Pa. Meanwhile, for 1 mm slot heights, the penetration factors were near unity for the majority of the particle size distribution. Their results matched closely with models they created from analysis of particle penetration through simplified cracks [Liu and Nazaroff, 2001] and had similar qualitative conclusions to Lewis's work.

Mosley studied particle penetration through a 0.508 mm slot height between aluminum plates with particles of aerodynamic equivalent diameters (AEDs) from 0.1 to 5 µm [Mosley *et al.*, 2001]. They found penetration factors close to unity for particle sizes between 0.1-1 µm, with a sharp drop-off in penetration factor for particle sizes larger than 1 µm for pressure differentials between 2 and 20 Pa – this was consistent with Liu and Nazaroff's results when considering the order of magnitude of the pressure differentials and particle size distributions.

The motivation behind the above work was based on ambient particle penetration of enclosures and the number of particles subject to human exposure, with slot heights and pressure differentials corresponding to conditions typically associated with building cracks and pressure differences between indoor and outdoor environments, respectively.

Casella studied the flow from pinhole breaches and particle deposition inside the breach for canisters with moderate pressure backfills [Casella *et al.*, 2006, Casella *et al.*, 2007]. The pinholes examined in these studies were relatively small, with diameters on the order of 10 µm. The particulates considered were also relatively small, with diameters of 0.05 to 0.1 µm. The initial, internal canister backfill pressure was 188 kPa. These analytic studies demonstrated that the effect of channel plugging can greatly reduce the leak rate from a canister.

However, the channel dimensions considered do not apply to the channel geometry associated with SCCs from potential corrosion of dry casks. The literature reports typical crack heights to be around 16 to 30 µm [EPRI, 2014 & 2017; Meyer *et al.*, 2016] and internal pressures of 100 to 760 kPa (14.5 to 110 psig) [EPRI, 2017] for a range of cask models. Therefore, an apparatus and procedures were developed to investigate a slot height on the order of 10 µm and pressure differentials on the order of 100 kPa to supplement the established database of particulate transmission in microchannel flows. This experimental approach has demonstrated adaptability for future testing of more prototypic stress corrosion crack geometries. Preliminary results using air as the carrier gas indicated 44% of the aerosols available for transmission were retained upstream of the microchannel [Durbin *et al.*, 2018].

1.3 Current Study and Collaborative Modeling

1.3.1 Uniqueness of Current Study

An aerosol spectrometer is utilized for this study to measure the size resolved aerosol concentration, also known as aerosol size distribution. The Palas Promo 3000 HP is fiber-optically coupled to two Welas 2200 high pressure aerosol sensors. The high-pressure aerosol sensor directly samples gas streams at native pressures up to 1.0 MPa. Rapid fiber optic switching allows a single instrument to analyze the upstream and downstream aerosol sensors in quasi-simultaneous fashion using the same optical detector. Switching of upstream and downstream sensors occurred every 10 seconds (see Section 2.3.4 for details). Thus, instrument bias was eliminated, and sample line losses were substantially minimized.

The uniqueness of this study from previous microchannel aerosol transport testing at Sandia National Laboratories (SNL) [Durbin *et al*., 2020] comes from the testing of a microchannel with a depth that varies linearly from 13 to 25 µm (more details in Section 2.2), which differs from the uniform 28.9 µm slot orifice tested previously. This choice of geometry is the next step following testing of a simple slot orifice as it is more representative of the microchannel profile that results from the evolution of a stress corrosion crack. Also unique to this study is the use of helium as a fill gas, which more closely represents a dry storage canister internal environment. The aerosol transmission through the linearly varying microchannel orifice was measured from tests using either helium or air as the fill gas at similar pressure differences between the upstream and downstream test sections. The procedure in which aerosols were introduced was kept as consistent as practical across tests for both fill gases. However, there were some procedural differences in the testing at the various final pressure levels when using helium versus air. Through this methodology, comparisons in aerosol transmission within two separate pressurized gas environments were made.

1.3.2 Collaborative Modeling Efforts

Modeling efforts from Pacific Northwest National Laboratory (PNNL) and Oak Ridge National Laboratory (ORNL) in collaboration with Purdue University are being conducted in parallel to the modeling and experimental efforts from Sandia National Laboratories. The focus of these efforts can be localized to two separate areas as illustrated in Figure 1.2.

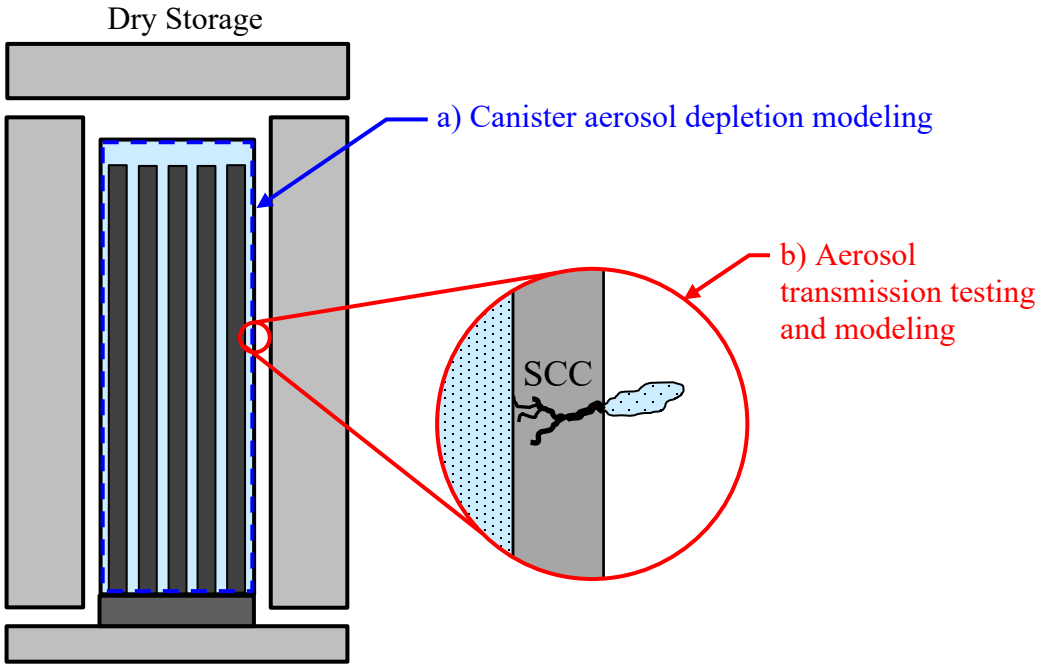

Figure 1.2 Collaborative modeling and testing areas.

GOTHIC modeling at PNNL [Lanza *et al*., 2021] and MELCOR modeling by Phillips and Gelbard at SNL [Phillips and Gelbard, 2021] focus on aerosol deposition within the canister internal volume (Figure 1.2*a*). First principles modeling of aerosol transport/depletion in microchannels by Chatzidakis at Purdue University and Sasikumar at ORNL [Chatzidakis and Sasikumar, 2021] and the experimental study presented in this report focus separately on aerosol transmission through a stress corrosion crack (Figure 1.2*b*). The modeling and experimental efforts running in parallel across multiple national laboratories will serve to develop further understanding of aerosol transport phenomena in DCSSs and SCCs.

2 APPARATUS AND PROCEDURES

The experimental approach adopted for these studies is similar to previous studies [Lewis, 1995; Mosley *et al.*, 2001; and, Liu and Nazaroff, 2001 and 2003] in that aerosol analyzers are used to characterize the particle size distribution and concentration present in the gas before and after flowing through a simulated crack. Because these previous studies considered aerosol transport through building walls or containment structures, the focus was on flows through relatively wide and long slots driven by constant low pressure drops. In the present study, consideration was given to aerosol transport through dry storage canister walls. Here, the focus was on a much narrower and shorter microchannel that represents a stress corrosion crack through the canister wall with aerosol transport driven by initially higher pressure drops across the wall.

Two types of tests were considered for these studies. In the first test type, denoted as a "blowdown," the storage tank was pressurized, isolated from the pressure source, and allowed to blowdown to ambient pressure via the microchannel. In the second test type denoted as "constant pressure," the pressure in the storage tank was maintained at a constant value with a pressure controller as flow is directed through the microchannel. The blowdown type of test more closely simulated the expected behavior of a pressurized SNF canister. While not prototypic, the constant pressure tests decoupled the pressure transient, which allowed better examination of the SCC discharge characteristics as it was fouled with deposited particulates.

2.1 General Construction and Operation

The general layout of the experimental setup is illustrated in Figure 2.1 and Figure 2.2. A 0.908 m^3 (240 gal) pressure tank is used to simulate the canister. Canisters typically have internal free volumes of approximately 6 m^3. Several stirring fans were installed roughly along the tank centerline to stir the particulates and minimize aerosol depletion over the course of a test. The tank was initially loaded with a measured quantity of dry powder aerosols using a Palas rotating brush generator (RBG), see Section 2.3.5 for more details on the RBG. The reference aerosol concentration at STP was 54 mg/m^3 in the upstream test section (see Section 2.4.2). Excess powder was loaded into the pressure tank, but this level of aerosol loading in the upstream test section was difficult to achieve. The RBG could operate with either air or helium at differential pressures up to 200 kPa. This meant that for the two higher pressure tests, the pressure tank was subsequently pressurized to the final test level. The flow rate and pressure drop were established through the test section using a clean background gas. The clean air supply to the pressure tank was then turned off, and each test was initiated with the opening of the 2-inch ball valve, allowing aerosols to begin entering the test sections.

Gas flow leaving the test section and exhausting to ambient was measured as was the flow drawn into each of the aerosol sensors. The engineered microchannel, simulating a crack, was mounted in the middle of the test section comprised of mounting flanges and two 0.61 m (24 inch) long, 0.10 m (4 inch) diameter schedule 40 pipe nipples. A sample stream was drawn from the centerline at the nipple midpoint (0.30 m from the microchannel) on the high-pressure upstream and low-pressure downstream sides of the test microchannel for aerosol size and concentration characterization using identical Welas 2200 high pressure aerosol sensors monitored by a single Palas Promo 3000 HP analyzer. Mass flow meters measured the sample flow leaving each of the aerosol sensors. Gas flow from the tank and through the test section was measured by a mass flow meter downstream of the test section. Pressure was monitored on the upstream and downstream sides of the microchannel using pressure transducers. A low pressure drop, high-efficiency particulate absorbing (HEPA) filter was used to remove all aerosols from the exhaust stream before the final mass flow measurement.

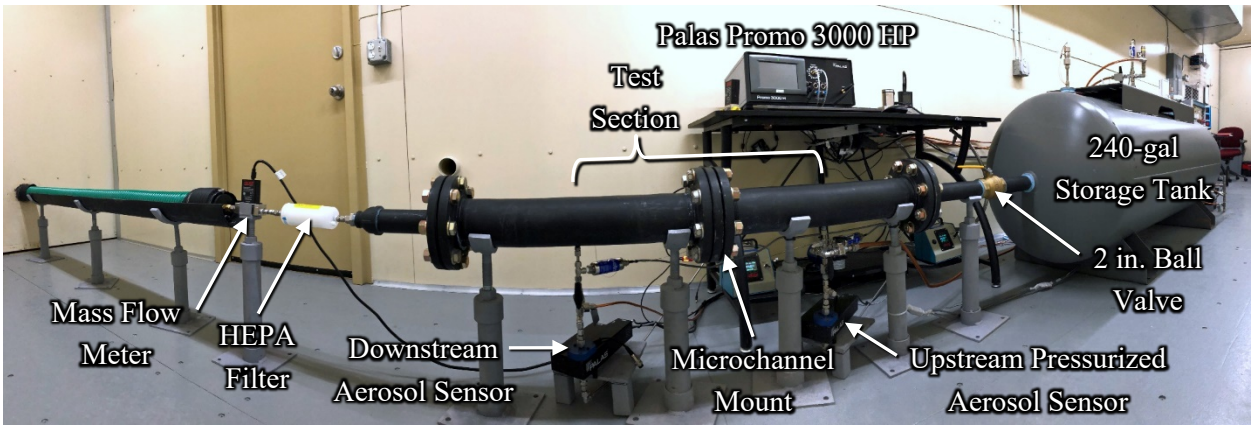

Figure 2.1 General layout of the experimental apparatus.

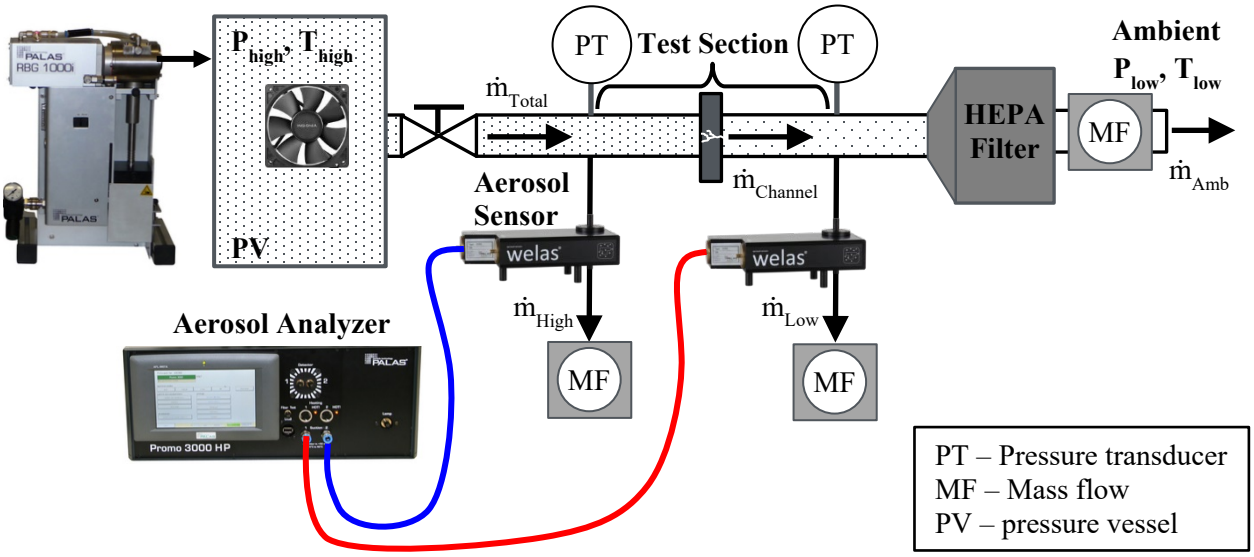

Figure 2.2 Schematic of the apparatus showing the major components.

2.2 Design of the Microchannel

The microchannel used in this study has a slot opening that gradually increases in a linear fashion from 13 µm to 25 µm, with the 13 µm depth facing the upstream portion of the test section as illustrated in Figure 2.3. The microchannel was fabricated from paired high-precision Mitutoyo gage blocks as shown in a schematic in Figure 2.4. The microchannel was formed by machining into the surface of one of the gage blocks using electrical discharge machining (EDM). The mounting holes were also cut using wire EDM. The paired halves of the gage blocks were bolted together to form the microchannel held in a mounting assembly as detailed in Figure 2.5. An isometric view of the microchannel mounted to the flow flange is shown in Figure 2.6.

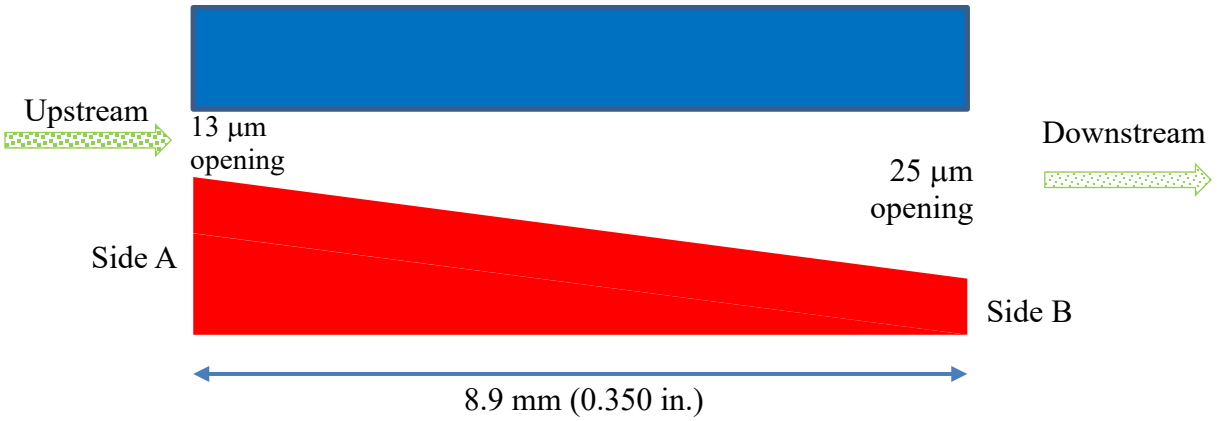

Figure 2.3 Illustration of the linear slot microchannel (not to scale).

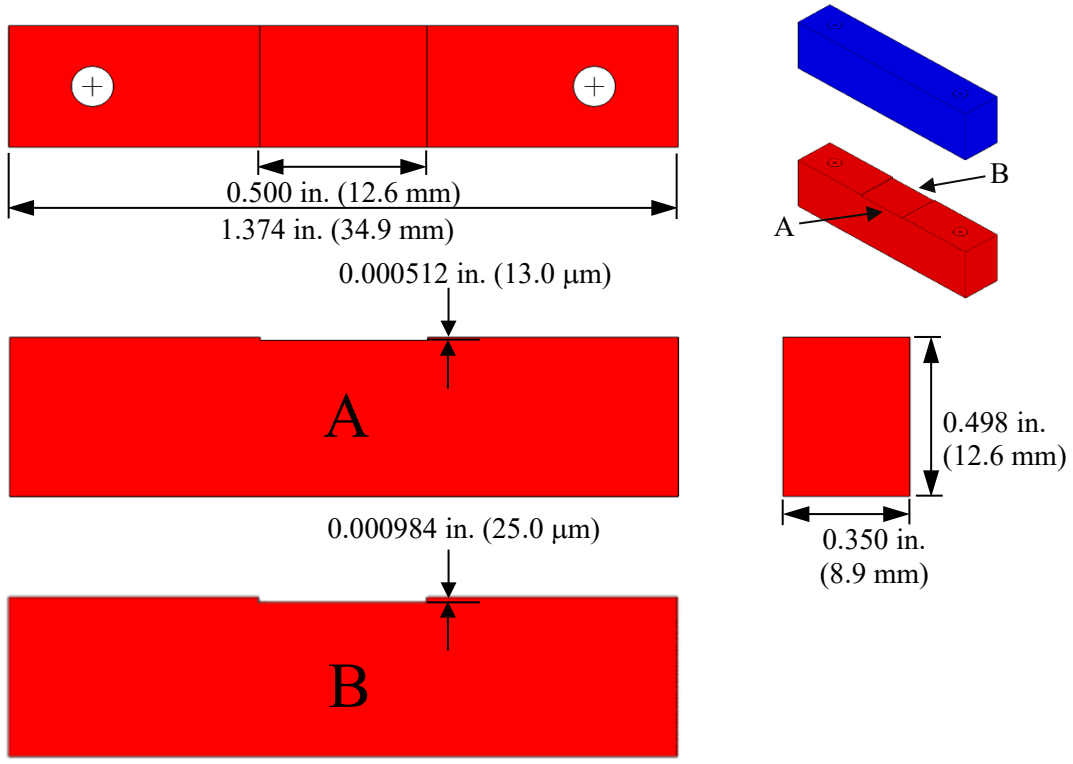

Figure 2.4 Schematic of the linear block (13 to 25 µm depth transition) microchannel assembly. Side A (13 µm depth) faces towards the upstream portion of the test section; side B (25 µm depth) faces towards the downstream portion.

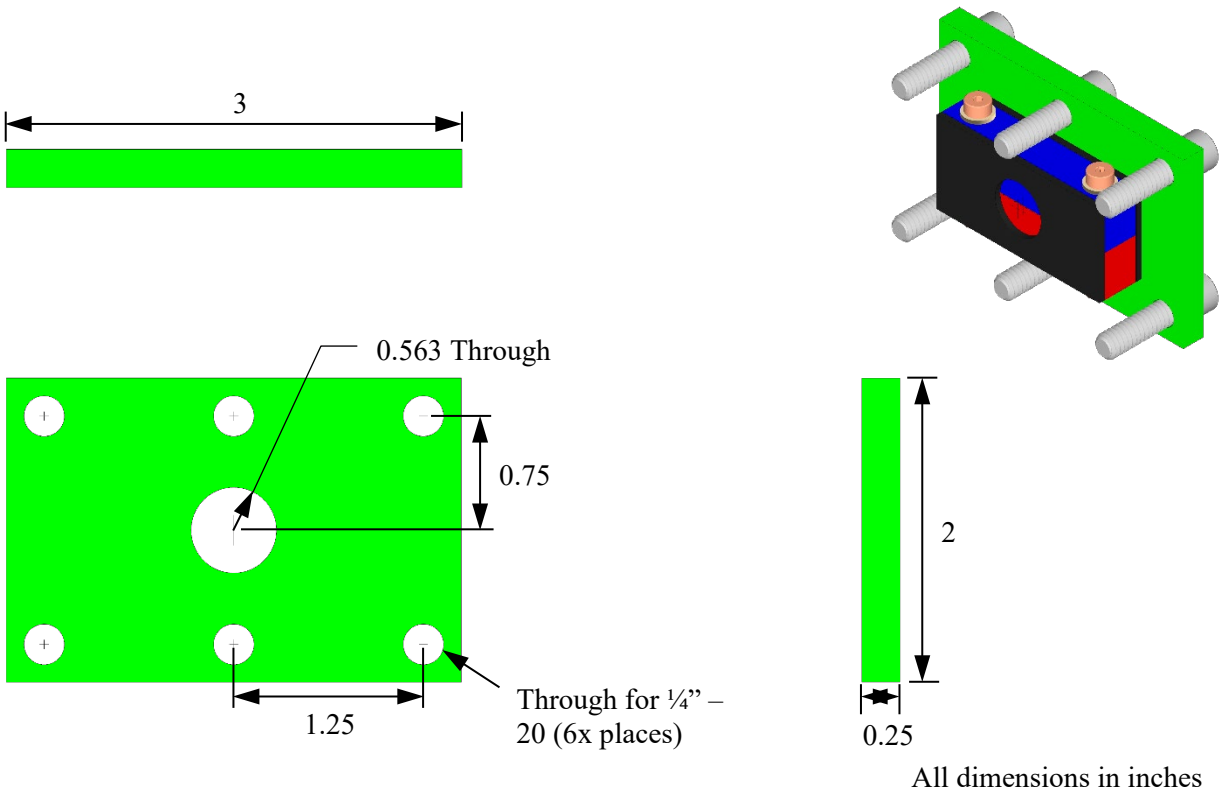

Figure 2.5 Details of the microchannel mounting assembly.

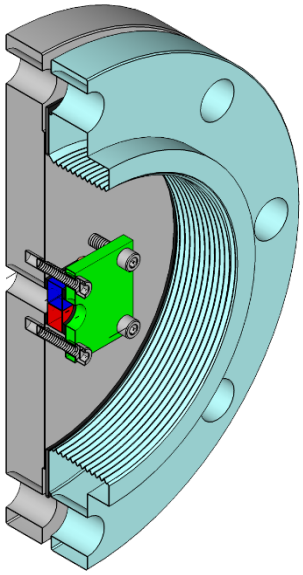

Figure 2.6 Isometric cutaway showing the microchannel mounted to the flow flange.

Figure 2.7*a* and Figure 2.7*b* show a profilometry image and a corresponding line scan along the flow path of the microchannel (shown in red) of the linear microchannel block, respectively. These profiles were taken with a Keyence VK-X100 laser scanning microscope.

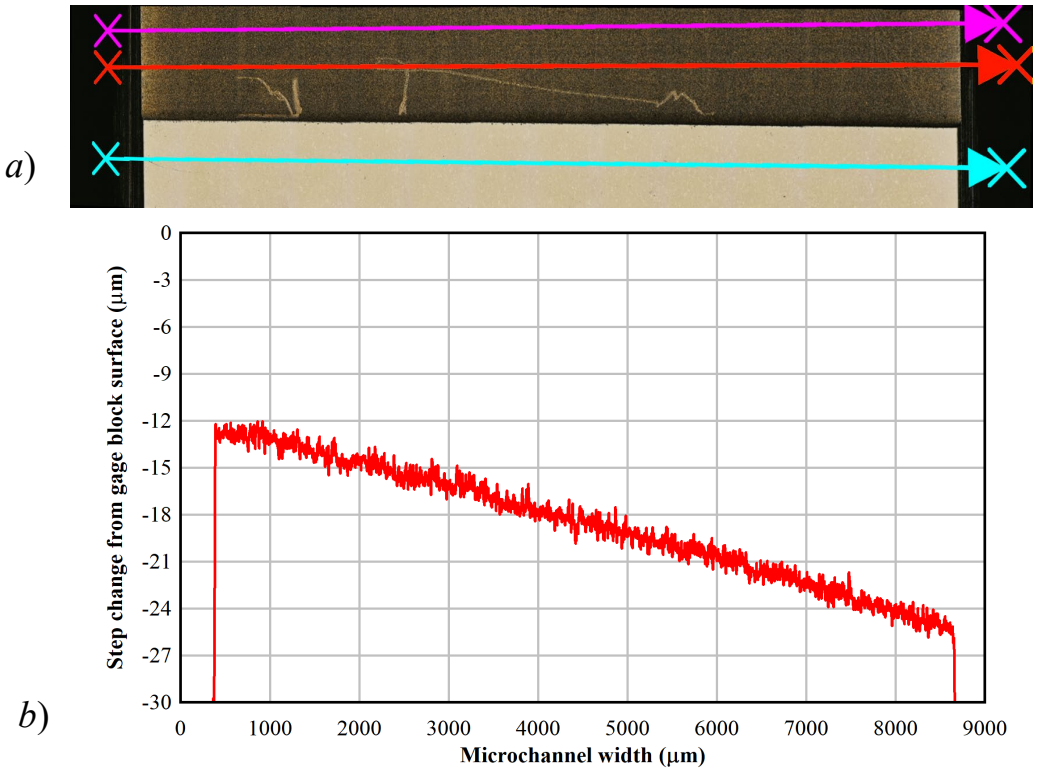

Figure 2.7 *a*) Profilometry image and *b*) line scan of the linear block (13 to 25 µm depth transition) microchannel using the Keyence laser scanning microscope.

The sharp drop-offs in Figure 2.7*b* of the microchannel block represent the start of chamfers along the edges of the block and effectively define the beginning and end of the microchannel. Figure 2.8 shows these chamfers in more detail. The linear slope region spans 8.26 mm across the microchannel width, but the total width of the block is 8.89 mm, so 0.63 mm of the flow length is a chamfered region into and out of the microchannel.

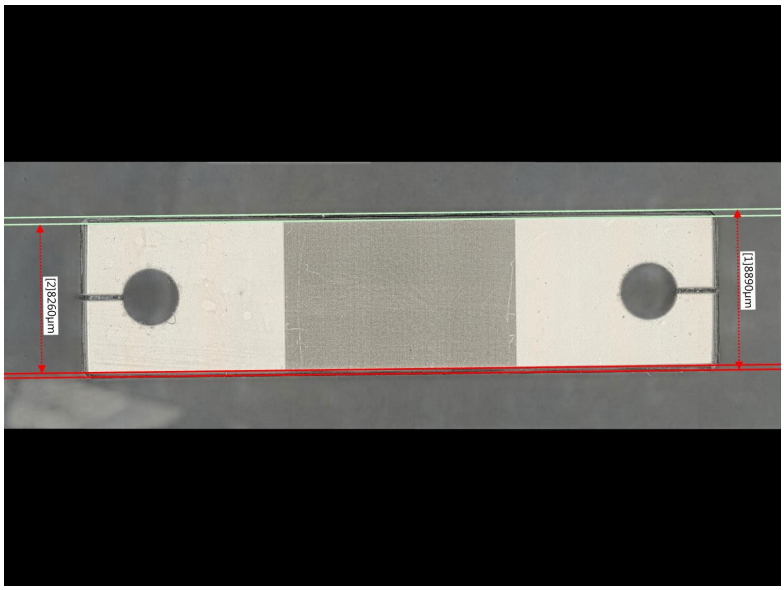

Figure 2.8 Optical microscope image of the linear block detailing the chamfered regions.

The surface roughness of the microchannel was also characterized with the Keyence VK-X100 laser scanning microscope as shown in Figure 2.9. The average arithmetical mean height (S_a) of the microchannel was found to be 0.734 µm, which was on the same order as the measured S_a values of the slot orifice microchannel used in previous testing (0.408 and 0.386 µm for the left and right sides of the microchannel region, respectively) [Durbin *et al*., 2020].

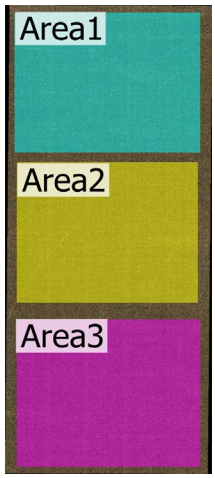

Figure 2.9 Surface roughness scans of the microchannel region. The average surface roughness was calculated from the surface roughness of the three areas shown.

2.3 Instrumentation

The following instrumentation was used to characterize these tests. All stated uncertainties are assumed to represent 95% confidence intervals unless otherwise stated.

2.3.1 Pressure

Pressure was monitored on the upstream side using a 1,034 kPa (150.0 psia) Setra Model ASM transducer and on the downstream side with a 103 kPa (15.0 psia) Setra Model ASM transducer. The pressure in the tank was monitored with a 2,068 kPa (300 psia) Setra Model ASM transducer.

The uncertainty of all the Setra pressure transducers is < ± 0.05% full scale (FS).

Table 2.1 Summary of pressure transducers.

Location	Model No.	Full Scale (kPa)	Uncertainty (kPa)
Storage tank	ASM1-300P-A-1M-2C-03-A-01	2,068	1.03
Upstream	ASM1-150P-A-1M-2C-03-A-01	1,034	0.52
Downstream	ASM1-015P-A-1M-2C-03-A-01	103	0.05

2.3.2 Temperature

All temperature measurements were taken with K-type thermocouples with standard calibration. The suggested, combined uncertainty in these measurements including data acquisition, cabling, and positioning errors is 1% of the reading in Kelvin [Nakos, 2004].

2.3.3 Mass Flow Rate

Flow from the test section was measured by a low pressure drop mass flow meter (Alicat, MW-20SLPM for $\Delta P \approx 420$ kPa and 720 kPa with air as the background gas, MW-10SLPM for $\Delta P \approx 420$ kPa and 720 kPa with helium as the background gas, and MW-2SLPM for $\Delta P \approx 120$ kPa with air as the background gas). Flow to the upstream and downstream (high pressure and low pressure) aerosol sensors was controlled by mass flow controllers (Alicat, MC-5SLPM). The standard liter per minute (slpm) is defined as one liter of air flow at standard temperature and pressure (STP) of 25 °C and 101.325 kPa (*i.e.* reference density of $\rho_{STP} = 1.184$ kg/m^3). The mass flow meters and controllers used during testing are presented in Table 2.2 and were chosen based on the best match between the starting mass flow rate of each test and the full scale of the mass flow meter.

For all the mass flow meters and controllers, the reported 95% uncertainty is ± (0.4% of reading + 0.2% FS) for a maximum of ± 0.6% FS.

Table 2.2 Summary of mass flow instrumentation.

Description	Model No.	Full Scale Q_{STP} (slpm)	Uncertainty (slpm)
High flow downstream exhaust	MW-20SLPM	20	0.12
Mid flow downstream exhaust	MW-10SLPM	10	0.060
Low flow downstream exhaust	MW-2SLPM	2	0.012
High pressure aerosol sensor	MC-5SLPM	5	0.030
Low pressure aerosol sensor	MC-5SLPM	5	0.030

2.3.4 Aerosol Spectrometer

The Palas Promo 3000 HP is a flexible, light-scattering aerosol spectrometer system that uses twin optical sensors to determine quasi-simultaneous particle concentration and particle size at two locations. Fiber-optic cables (light wave conductor or LWC) are used to carry light from the main controller to the remote Welas 2200 high pressure aerosol sensors as well as the resulting light-scattering signal from the remote sensors back to the main controller. The Welas 2200 sensors are specially designed to require only 0.5 actual liters per minute (alpm) of flow. This high-pressure aerosol sensor is capable of directly measuring samples at pressures up to 1000 kPa. Rapid fiber optic switching allows a single instrument to analyze the upstream and downstream aerosol sensors in quasi-simultaneous fashion.

The instrument collected data from the upstream sensor for 50 seconds in ten-second increments, generating five upstream data points (each consisting of a 10 second average concentration and corresponding 64-channel number count distribution). The switch to the downstream sensor required ten seconds, and then the instrument collected data from the downstream sensor generating another five downstream data points. The nature of the data stream is therefore a series of five data points at 10 second intervals followed by a 60 second gap in data while the other sensor was analyzed.

The aerosol spectrometer characteristics are summarized in Table 2.3. This sensor range makes reliable measurements possible over a concentration range from 1 to 10^6 particles/cm^3. The instrument is ideally suited to simultaneously monitor the aerosols from the high-pressure upstream and low-pressure downstream side of the simulated crack for aerosol size and concentration characteristics.

Table 2.3 Summary of the aerosol spectrometer capabilities.

Instrument Characteristic	Value
Aerosol size range	0.3 to 17 µm
Aerosol size channels	64/decade
Minimum Particle Concentration	1 particle/cm^3
Maximum Particle Concentration	10^6 particles/cm^3
Maximum Sample Pressure	1,000 kPa
Maximum Sample Temperature	120 °C

2.3.5 Aerosol Generator

The aerosols were loaded into the pressure tank with a Palas rotating brush generator RBG 1000 (Figure 2.10*a*) to initialize the test using the desired background gas at a differential pressure of up to 200 kPa. The RBG 1000 can deliver particles at a rate between 40 mg/h to 430 g/h. The heart of the instrument is the rotating brush (Figure 2.10*b*). The desired aerosols to be dispersed are packed into a cylinder. A transport piston slowly pushes the bed of packed powder into the rotating metal bristle brush that dislodges particles and holds them in the bristles. When the brush rotates 180 degrees further, the bristles are exposed to a flow of dispersion carrier gas that suspends the particles and transports them away, creating a polydisperse distribution of desired aerosol.

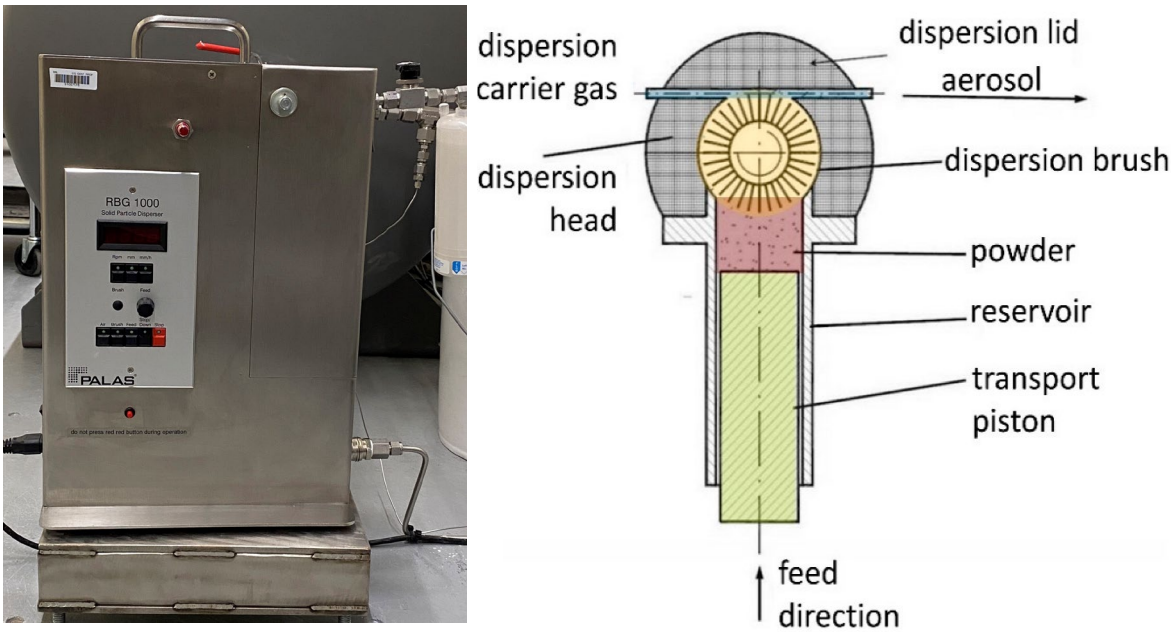

(*a*) (*b*)

Figure 2.10 (*a*) Image of the Palas RBG 1000 and (*b*) diagram of the rotating brush. [Palas GmbH, 2002]

2.4 Aerosol Characteristics

2.4.1 Selection of Surrogates

Cerium oxide (CeO_2) was chosen as the surrogate for spent nuclear fuel ($\rho_{SNF} \approx 10$ g/cm^3) because of its relatively high density ($\rho_{CeO2} = 7.22$ g/cm^3) and its commercial availability. For cerium oxide, an AED particle size of 10 µm equates to a geometric particle size of 3.72 µm. Geometric particle size is used exclusively through the remainder of this report. Figure 2.11 shows the particulate sizes as characterized

by the probability distribution function (PDF) and cumulative distribution function (CDF) of the surrogate used in these tests. Here, the distributions are plotted as a function of geometric diameter (bottom) and AED (top). This specific lot of CeO_2 was chosen because the particulates were concentrated in the respirable range (AED < 10 µm). The mass median diameter (MMD) was 2.4 µm (or MMD_{AED} = 6.4 µm), the geometric standard deviation (GSD) was 1.9, and ~75% by mass of the particles was respirable (AED < 10 µm). Fifty percent of the measured particles have a mass smaller than the MMD (also known as D_{50}), and 50% of the measured particles have a mass that is greater.

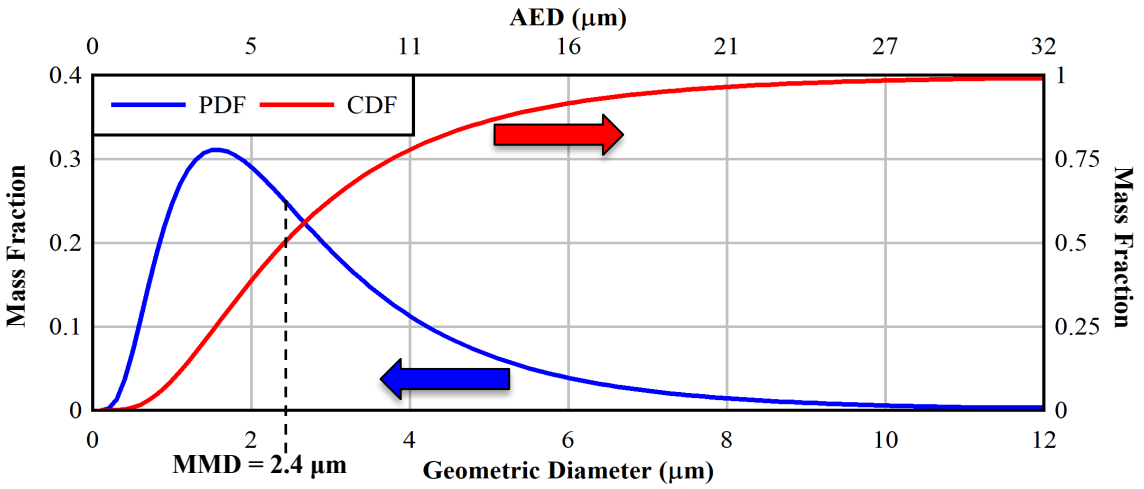

Figure 2.11 Size distributions of the cerium oxide surrogates used in testing.

2.4.2 Reference Initial Aerosol Concentration

The particulates released from SNF were characterized when air was forced through segmented fuel [Hanson *et al.*, 2008]. The geometric particle size data from nine tests conducted on four fuel rod segments are summarized in Figure 2.12. The average of the nine tests yielded an MMD of 3.46 µm (geometric diameter), a GSD of 2.24, a total release fraction of 1.9×10^{-5} of which 46% was respirable for a respirable release fraction of 8.9×10^{-6}. This respirable release fraction is in reasonable agreement with 4.8×10^{-6} cited in NUREG-2125 [NRC, 2012] and 3×10^{-6} cited in SAND90-2406 [Sanders, *et al.*, 1992].

To estimate an upper aerosol density for spent fuel dry storage, a canister with 37 pressurized water reactor (PWR) assemblies with a fuel mass (UO_2) of 520 kg per assembly was assumed. One percent of the fuel was assumed to fail simultaneously due to an undefined event. The canister was assumed to have an internal free volume of 6 m^3 and a starting initial pressure of 800 kPa (116 psia). The equivalent aerosol density for this assumed system at STP is approximately $C_{m,\,STP}$ = 54 mg/m^3. For all testing described in this paper, the standard temperature and pressure were taken as the default values for the mass flow rate instruments (Alicat MC and MW Series) of 298.15 K (25 °C) and 101.353 kPa (14.7 psia).

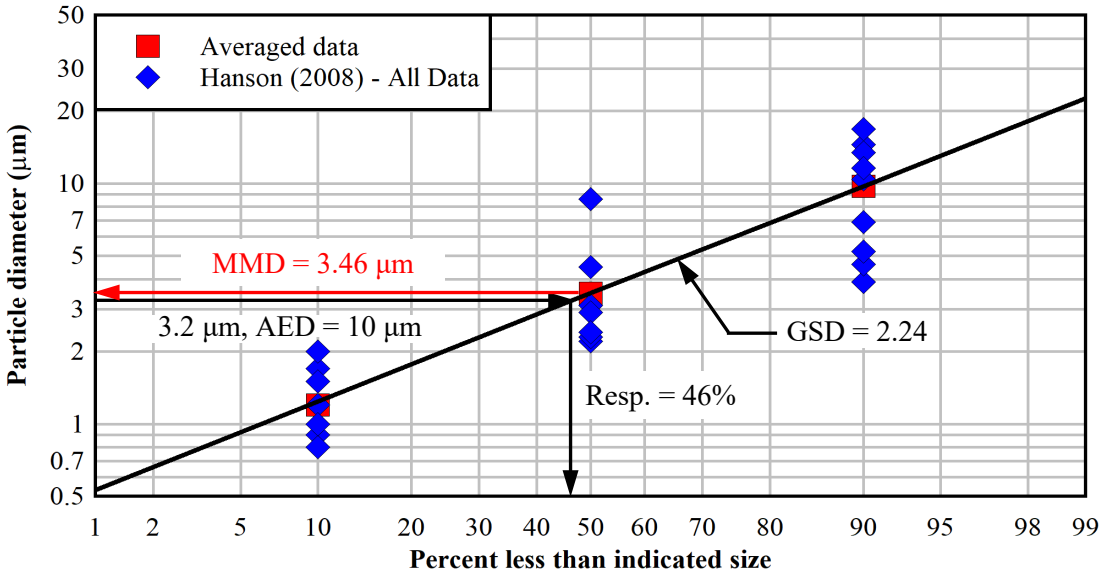

Figure 2.12 Respirable fraction of spent fuel from Hanson *et al.* 2008.

3 RESULTS

3.1 Clean Flow Tests

The mass flow rate characteristics of the engineered microchannel used in this study were first evaluated in the absence of aerosols. All clean flow tests were conducted with the Promo aerosol sensors off, to allow all gas to exhaust through the microchannel and exhaust pathway. The flow results with air and helium are summarized in Figure 3.1, which shows the air mass flow rate through the clean microchannel as a function of a wide range of pressure drops. Also shown for reference are the three initial pressure drops considered in the aerosol-laden tests: nominally 120 kPa, 420 kPa, and 720 kPa indicated by a solid diamond in black, blue, and red, respectively. The velocity through the microchannel is roughly the same for both gases at the same pressure differential, but the mass flow rates are significantly different because the density of air is greater than helium by a factor of roughly 7.2 for a given pressure. The average ratio of the measured mass flow of clean air and helium was 7.3 over the range of pressure differential values in Figure 3.1.

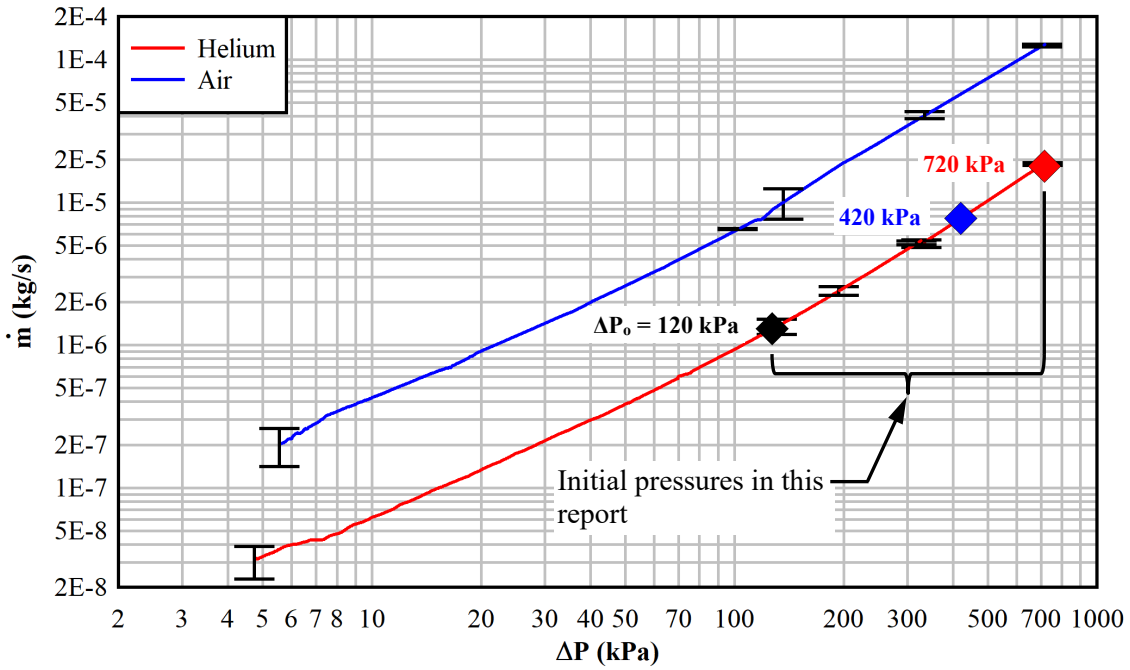

Figure 3.1 Mass flow rate as a function of pressure drop across the linear microchannel for helium (red line) and air (blue line).

3.2 Aerosol-Laden Flow Tests

3.2.1 Air Tests

As summarized in Table 3.1, a total of seventeen aerosol-laden air flow tests were conducted with up to three nominal initial pressure drops (120 kPa, 420 kPa, and 720 kPa) each for two test modes (blowdown and constant pressure) over a wide range of initial aerosol mass concentrations (18.7 to 141 mg/m^3). The final, integrated aerosol mass, M(τ), in the upstream and downstream sections are given for each test. In addition, the ratio of these values is reported as the integrated transmission. The methods for determining these values are defined in Section 3.2.3.

Table 3.1 Aerosol-laden flow test matrix summary of results for air.

Date	Test Type	ΔP_o (kPa)	Upstream Initial Conditions				Final		
			C_m (mg/m^3)	$C_{m,STP}$ (mg/m^3)	MMD (µm)	GSD (--)	M_{Down} (mg)	M_{Up} (mg)	Integrated Transmission
6/11/2021	Blowdown	119	18.7	9.26	1.4	1.8	0.09	0.20	0.473
5/6/2021	Blowdown	120	33.6	16.6	1.7	1.8	0.33	0.84	0.395
6/13/2021	Blowdown	415	24.5	4.90	1.7	2.0	0.44	0.79	0.550
6/12/2021	Blowdown	418	81.1	16.3	1.8	1.9	1.02	1.67	0.608
4/29/2021	Blowdown	716	20.1	2.55	1.7	2.1	0.43	0.90	0.473
6/2/2021	Blowdown	717	34.2	4.30	1.9	2.1	0.49	1.24	0.396
6/3/2021	Blowdown	723	44.2	5.60	2.0	2.0	0.73	1.66	0.437
6/8/2021	Blowdown	717	79.1	10.0	1.9	1.9	1.11	3.11	0.357
5/4/2021	Blowdown	717	81.4	10.4	2.0	2.0	1.85	3.74	0.495
4/28/2021	Blowdown	717	108	13.6	2.1	2.1	0.75	2.88	0.262
6/1/2021	Blowdown	717	115	14.6	2.2	2.0	1.51	3.76	0.400
6/9/2021	Blowdown	717	123	15.5	2.1	1.9	1.31	3.66	0.358
5/3/2021	Blowdown	717	134	16.8	2.2	2.2	1.22	4.33	0.282
5/26/2021	Blowdown	717	141	17.9	2.4	2.1	1.76	5.71	0.309
6/10/2021	Constant Press.	717	25.2	3.10	1.7	1.9	0.52	1.26	0.409
6/7/2021	Constant Press.	714	89.3	11.1	2.1	2.0	1.35	4.06	0.333
6/4/2021	Constant Press.	716	119	14.8	2.2	2.1	1.57	4.45	0.353

3.2.2 Helium Tests

A total of thirteen aerosol-laden helium flow tests were conducted at the two highest nominal initial pressure drops (420 kPa and 720 kPa) primarily for the blowdown configuration over a wide range of initial upstream aerosol concentrations (35.8 to 273 mg/m^3) as shown in Table 3.2. At first inspection, the helium transmission results appear to be lower than those recorded for air. However, further study reveals that the integrated transmission appears to be highly proportional to the initial mass median diameter, MMD_o, which is a reasonable measure for the particle sizes at the start of the test when aerosol mass transmission is highest. The MMD_o for the helium tests is greater than comparable air tests at otherwise similar conditions. The reasons for this difference are currently not fully understood and are the subject of an ongoing investigation. Under consideration are minor differences in the test procedure details between using air or helium at the various pressures and the impact on mixing and settling times in the pressure tank. Further combined analyses of the air and helium results are available in Section 3.2.4.

Table 3.2 Aerosol-laden flow test matrix summary of results for helium.

Date	Test Type	ΔP_o (kPa)	Upstream Initial Conditions				Final		
			C_m (mg/m^3)	$C_{m,STP}$ (mg/m^3)	MMD (μm)	GSD (--)	M_{Down} (mg)	M_{Up} (mg)	Integrated Transmission
6/25/2021	Blowdown	418	35.8	7.20	2.3	1.9	0.26	0.84	0.316
6/24/2021	Blowdown	417	121	24.3	2.8	1.9	0.49	1.91	0.260
6/30/2021	Constant Press.	417	61.1	12.1	2.6	2.0	0.49	1.32	0.371
6/29/2021	Constant Press.	418	114	22.7	2.5	2.0	0.71	2.67	0.266
7/13/2021	Blowdown	716	43.0	5.43	1.7	2.0	0.90	1.94	0.466
6/28/2021	Blowdown	717	74.8	9.40	2.9	1.9	0.73	3.12	0.234
6/20/2021	Blowdown	739	82.5	10.1	2.5	1.9	0.74	2.81	0.264
6/17/2021	Blowdown	713	86.8	11.0	2.2	1.8	0.76	3.67	0.208
6/21/2021	Blowdown	716	139	17.5	2.7	1.9	1.06	4.62	0.229
6/19/2021	Blowdown	719	224	28.0	3.1	2.0	1.27	8.18	0.155
6/29/2021	Blowdown	715	273	34.2	3.5	1.9	1.06	8.91	0.118
6/18/2021	Constant Press.	716	66.4	8.26	2.6	1.9	0.70	2.62	0.266
6/16/2021	Constant Press.	720	193	24.0	2.4	1.9	1.28	7.20	0.178

3.2.3 Data Analysis

The measured instantaneous mass rate of aerosols upstream or downstream of the microchannel at any time t may be expressed as shown in Equation 3.1. Here, the mass flow rate of the background gas, Q_{STP} in units of m^3/s, at time t is multiplied by the mass concentration of aerosols, $C_{m,STP}$ in units of mg/m^3, at the same time t, both at STP conditions. The instantaneous transmission at time t is defined as the mass rate downstream divided by the corresponding instantaneous mass rate upstream as shown for the complementary instantaneous retention in Equation 3.2. The integrated mass transmitted to and from the microchannel is calculated as the integral of the instantaneous mass rate from a lower limit of t_o = 0.1 hours to an upper limit governed by the available aerosol data (τ) as shown in Equation 3.3. The initial offset in the integration limit of 0.1 hours is to account for the short delay in flow of aerosols from the storage tank into the test section. By taking the ratio of the downstream to the upstream integrated mass of aerosols, the integrated transmission of aerosols through the microchannel may be estimated (Equation 3.4). Because the mass flow of gas through the microchannel is conserved in the upstream and downstream calculation in Equation 3.1, the flow cancels in the calculation of the integrated transmission in Equation 3.4. Inherent assumptions are minimal aerosol wall and flow flange impaction losses between the upstream and downstream sample locations and quasi steady-state flow upstream and downstream of the microchannel.

$$m(t) = Q_{STP}(t) \cdot C_{m,STP}(t) \text{ [Units = mg/s]} \quad \textbf{3.1}$$

$$\text{Instantaneous Retention} = 1 - m_{Down}(t) / m_{Up}(t) \quad \textbf{3.2}$$

$$M(\tau) = \int_{t_o}^{\tau} m(t)\,dt \text{ [Units = mg]} \quad \textbf{3.3}$$

$$\text{Integrated Transmission} = M_{Down}(\tau) / M_{Up}(\tau) \quad \textbf{3.4}$$

3.2.3.1 Aerosol Concentration

Transmission of particulates through the microchannel was determined directly by measuring the aerosol concentration contemporaneously both upstream and downstream of the microchannel. To facilitate this analysis, the raw temporal concentration data were fit to a fourth order log-log polynomial prior to the

integration. Figure 3.2 shows an example of the upstream and downstream concentration transients and curve fits for the air blowdown test conducted on June 1, 2021. The upstream aerosol concentration drops nearly three orders of magnitude over twelve hours indicating aerosol depletion in the pressure tank. The concentration of aerosol for any given time is greater upstream than downstream indicating the microchannel was acting as a filter. The concentration difference between upstream and downstream is greatest initially and the two concentrations asymptotically approach each other at later times. For all tests, the start of the test (t = 0 hours) is marked by the opening of the 2 in. ball valve to the storage tank releasing aerosols to the microchannel. An additional, temporal correction was needed to synchronize the samples because of the transit time of the carrier gas from the upstream to the downstream sample ports. This correction was approximated by shifting the downstream data earlier in time based on the time required to displace the volume of gas between the upstream sampling port and the microchannel. The typical time shift was on the order of minutes.

Figure 3.3 shows a typical result of the integrated aerosol masses for the upstream and downstream sections on the left dependent axis for the test conducted on June 1, 2021. The ratio of the downstream to the upstream aerosol mass, *i.e.* integrated transmission, is shown on the right dependent axis. Although care was taken to accommodate the stabilization of the aerosol concentrations at the start of the test, the combination of curve fitting and the selection of a test-independent lower integration limit, t_o = 0.1 h, led to some integrated transmissions displaying initial, non-monotonic behavior at elapsed times less than half an hour.

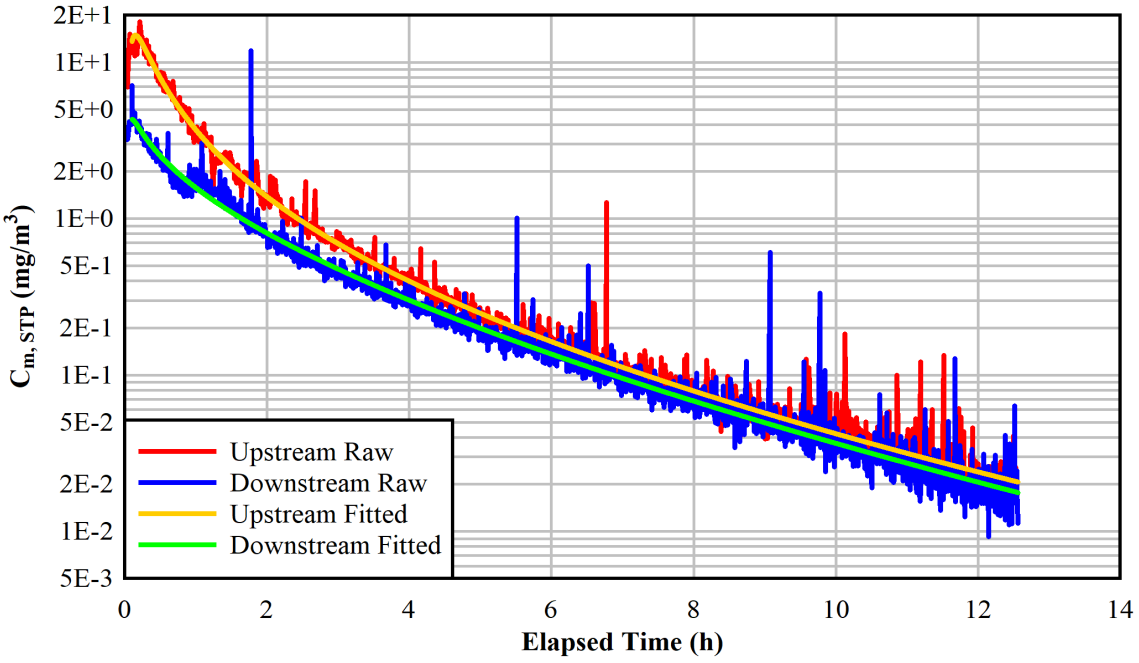

Figure 3.2 Raw and curve-fit aerosol mass concentrations for the air blowdown test conducted on 06/01/2021 with ΔP_o = 717 kPa and an initial upstream concentration of $C_{m, Up, STP, o}$ = 14.6 mg/m^3 ($C_{m, Up, o}$ = 115 mg/m^3).

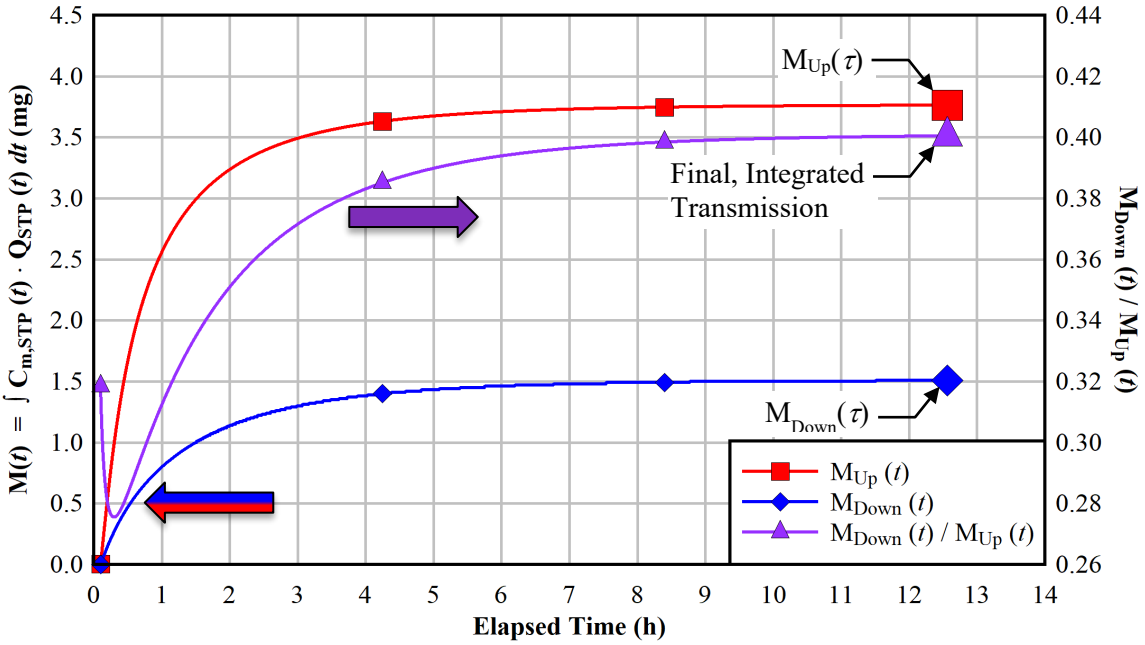

Figure 3.3 Integrated aerosol mass concentrations for the air blowdown test conducted on 06/01/2021 with ΔP_o = 717 kPa and an initial upstream concentration of $C_{m,\,Up,\,STP,\,o}$ = 14.6 mg/m^3 ($C_{m,\,Up,\,o}$ = 115 mg/m^3).

3.2.4 Comparison of Air and Helium Aerosol Transmissions

The transmission behavior of the aerosols suspended in air and helium are very similar. Figure 3.4 shows the measured transmission of aerosol mass through the linear slot orifice as a function of the initial MMD_o for both air and helium used as the fill gas. Air (blue squares) and helium (red diamonds) tests are shown together in the graph. The data show an inverse relationship such that the transmission is high when the MMD_o is small and the transmission is low when the MMD_o is large. This behavior is observed for both fill gases tested, suggesting independence of gas type. While more testing is needed to verify this apparent independence, the potential to conduct the majority of tests with air is highly attractive because of experimental ease and cost.

The estimated particle size distribution from spent fuel testing MMD_o = 3.46 µm [Hanson *et al.*, 2008] is represented by the last data point in the graph. For this starting particle size distribution, the integrated transmission is ~0.12. In order to better apply the techniques developed for these studies to the hypothetical transmission of fuel particulates through an SCC, future work must consider the expected aerosol depletion within the canister and other transient factors on the available particulates. To this end, modeling of the canister internals and evolution of aerosols after a release from the fuel to the interior has started in order to inform and synchronize with this research. These modeling efforts are described in the next chapter.

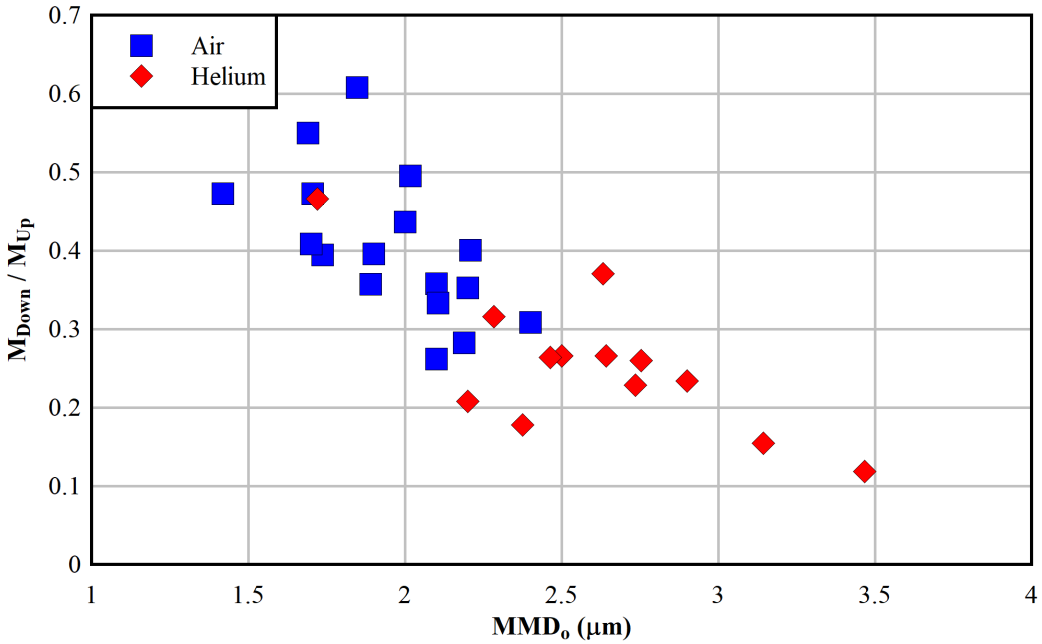

Figure 3.4 Integrated transmission as a function of initial mass median diameter.

4 CANISTER AEROSOL DEPLETION MODELING

Preliminary transient depletion of aerosols in a commercial spent nuclear fuel dry storage canister was independently modeled using two codes, MELCOR and GOTHIC. Some discrepancies in these predictions are likely due to differences in the initial conditions imposed by each code. An effort to refine these initial conditions and synchronize the codes for better comparisons is planned for future work. A brief, high-level summary of the modeling efforts is presented in subsequent subsections.

For both codes the aerosols are those defined in Section 2.4.2 with a density of 10.97 g/cm^3 and a lognormal size distribution with a mass median diameter of 3.46 μm and a geometric standard deviation of 2.24 μm. Three initial aerosol concentrations were considered, nominally 200 mg/m^3, 40 mg/m^3 and 4 mg/m^3, in helium at a pressure of 811 kPa and average temperature of 486 K for MELCOR and 701 kPa and 483 K for GOTHIC.

4.1 MELCOR

The MELCOR computer code [Humphries, 2018] couples thermal-hydraulic modeling and risk significant phenomena within a system level accident analysis code. While the documented MELCOR cask model is presently computing the thermal-hydraulic response and steady state system performance of the simplified cask, these calculations are intended to eventually be replaced with the ANSYS/Fluent® thermal-hydraulic results to improve the natural circulation modeling while restricting the MELCOR analysis to the computation of the aerosol phenomena.

MELCOR computes advection of mass and energy from arbitrary regions, defined by control volumes, by solving a three-equation set: mass, energy, and momentum for a hydrodynamic field. The code models transport for two fields, atmosphere and liquid, giving a total of six equations. In general, control volumes are used to define the hydrodynamic state of a given enclosed space. The altitude (top and bottom elevations) and total hydrodynamic volume are the principal input along with the initial thermal-dynamic information to satisfy the determination of the state parameters, pressure, temperature, constituent gas composition, and other parameters.

The canister is divided into 4 general regions, the top (region above the basket assembly), base (region below the basket assembly), the basket assembly (volume within the basket assemblies), and the fuel assemblies (the sub-region of the basket assembly that contains fuel pins). The fuel assemblies are subdivided into 5 axial segments, similar to reactor modeling practices [Bixler, 2013]. Plena are used to model the base and top regions, *i.e.* the header spaces below and above the basket assembly, respectively. These control volumes provide the inlet to and outlet from the basket assembly as well as the annulus region. Between the basket assembly and the canister inner wall is the annulus region, which is subdivided at the same axial positions as the basket assembly. Similarly, each annulus volume is connected to its nearest annulus neighbor by an inlet and outlet flow path.

MELCOR distinctly models intact structures with simple geometries, such as rectangular, spherical, or cylindrical. The fuel/gap/clad system is modeled with the dimensional characteristics of fresh fuel, the characteristic dimension is the outer diameter of the cladding for the cylindrical geometry. Default code behavior is maintained concerning the convection heat transfer regimes, natural versus forced flows, and flow regimes (laminar versus turbulent). Given the passive operation of the cask system, heat transfer will be continuously modeled with laminar/natural convection correlations for all heat structures.

Aerosolized UO_2 is sourced into the model to a prescribed size bin and total mass for the canister. This insertion occurs over a single timestep across all control volumes to produce a uniform concentration. Once the aerosol mass is present, MELCOR will compute the agglomeration and deposition rate of the UO_2 mass. By default, all aerosols are assumed to be adequately represented with a density of 1,000 kg/m^3. For light water reactor applications, where accidents involving large quantities of water are present, this assumption is well-founded. However, given a dry cask and assumed UO_2 aerosol, the

default density was specified as 10,980 kg/m^3, the density of UO_2. Further details of this modeling effort are recorded in an earlier report [Phillips and Gelbard, 2021].

4.2 GOTHIC

GOTHIC™ (Generation of Thermal Hydraulic Information in Containment) is an integrated finite volume, general-purpose thermal-hydraulics software package for design, licensing, safety, and operating analysis of nuclear power plant containment, confinement buildings, and system components licensed by EPRI and maintained by Zachry Nuclear Engineering [GOTHIC, 2018]. GOTHIC solves the conservation equations for mass, momentum and energy for multicomponent, multi-phase flow in lumped parameter and multidimensional geometries (1, 2, or full 3D), including the effects of turbulence, diffusion and buoyancy. The diverse equation set allows GOTHIC to solve multi-physics problems and the flexible nodalization options allows GOTHIC to provide computationally efficient solutions for multi-scale applications.

The primary fields in GOTHIC include steam/gas mixtures, continuous liquid, and multiple aerosol fields. Optional secondary fields are for ice, mist, and liquid components (particles suspended in drops and continuous liquid). Heat transfer is calculated between phases, and between surfaces and the fluid. Intrafield heat and mass transport allow for thermal non-equilibrium and closure relationships for intrafield momentum conservation allow for non-equilibrium velocities between gas and one or more aerosol fields. The code also has a feature to allow users/developers to add or modify equations for special calculations.

GOTHIC uses a log-normal size distribution characterized by an average particle diameter and GSD in each cell. The interface heat and mass transfer and interface drag are characterized by the Sauter mean diameter (SMD) for the field. The aerosol dynamics model solves particle count and surface area densities considering aerosol sources, agglomeration, and deposition. The agglomeration mechanisms in GOTHIC include thermal diffusion, turbulent shear, and gravitational collection and it is assumed that these mechanisms operate independently and that the total agglomeration rate is the sum of the rates for the individual mechanisms. The deposition mechanisms in GOTHIC include deposition due to gravitational settling, impaction, thermal and turbulent diffusion, thermophoresis, and diffusiophoresis, and it is assumed that these mechanisms operate independently and that the total deposition rate is the sum of the rates for the individual mechanisms. The deposition models are applied to each drop field separately.

PNNL has continued work to develop an aerosol-laden flow modeling capability with the GOTHIC computer code to perform simulations for thermal hydraulic conditions and aerosol transport and deposition in spent fuel casks [Lanza, *et al.*, 2019]. The model has been expanded to allow for thermal characterization, carrier gas velocity characterization, and tracking of particulate behavior throughout the entire canister volume. The expanded model capability was achieved through conversion of radioactive decay heat source in all fuel tubes within the model from heaters to thermal conductors in GOTHIC as well as remeshing the internal volume of the canister. In GOTHIC, heaters are used as a tool to specify heat sources within specified regions of the model, while thermal conductors allow for GOTHIC to couple the fuel pin and helium gas energy equations to calculate temperature of fuel and helium gas with decay heat source and heat transfer at the fuel clad-He gas interface. These improvements allowed for temperatures, carrier gas velocities, and particulate concentrations to be determined throughout the entire model space, which was not possible in the previous version of the model. Ultimately, the current version of the code is capable of tracking temperatures, flow rates, and particle behavior throughout the canister internal volume. Further details of GOTHIC modifications and modeling details for these efforts are available in an earlier report [Lanza *et al.*, 2021].

4.3 Canister Aerosol Depletion Model Comparisons

Figure 4.1 shows the transient aerosol depletion for both the MELCOR and GOTHIC model predictions at high, medium, and low aerosol concentrations for initial log-normal aerosol size distributions with

MMD = 3.46 µm and a GSD = 2.24. To facilitate the comparison, the peak aerosol concentration for the two models were translated to the same initial time of 10 s (or 0.028 h). The results from both codes show a significant depletion of aerosols with time. The MELCOR results indicate a faster drop in aerosol concentration at early times compared to the GOTHIC results, which give sharper drops at later times. After one to two hours, the results from both codes suggest that the initial aerosol loading has depleted by 3 to 6 orders of magnitude. Note that the abrupt plateauing of the aerosol concentration in the GOTHIC results is due to the count density dropping below the minimum count density of 1 particle per milliliter imposed by GOTHIC.

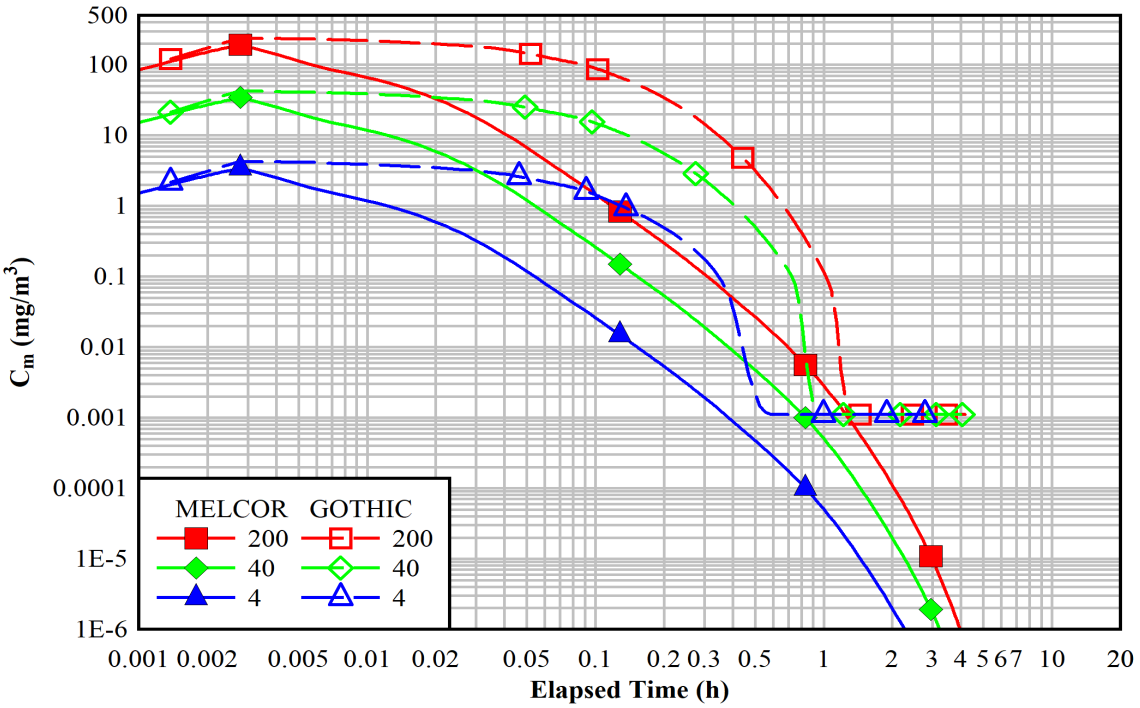

Figure 4.1 Comparison of aerosol depletion calculated by MELCOR (solid symbols) and GOTHIC (open symbols).

4.4 Comparison of Modeled Canister and Current Experimental Depletion Rates

Figure 4.2 shows the transient, normalized aerosol mass concentrations for the MELCOR and GOTHIC canister models in comparison to representative experimental depletion measured in the upstream test section. The comparison to the experimental data is useful as a bounding case of minimized depletion. The aerosol concentration is normalized by the peak concentration in each case.

The initial aerosol depletion observed in the experiments tracks closely with the GOTHIC predictions for several minutes after which the canister model depletion rate exceeds the experimental rate. Recall that the CeO_2 surrogate used in the testing has a lower density (ρ_{CeO2} = 7.22 g/cm^3) than SNF and the experimental aerosol tank was designed to minimize aerosol depletion. These designs include minimizing internal surface area that promote deposition and the deployment of fans inside the mixing tank that offset gravitational settling (see Section 2.1).

In general, the deposition of the SNF aerosols within the first few hours greatly reduces the total mass concentration. Assuming that the failure of fuel pins results in an ejection of aerosolized SNF, the duration of particulates remaining in suspension appears to be relatively short. The bulk flow from

internal convection and fill pressure inside the canister would be largely unperturbed over these time scales by any flow exiting an SCC because the discharge would be relatively small. This comparison of initial modeling and current testing shows that the test setup, which has been designed to minimize depletion, may be creating conditions that are overly conservative for a prototypic system. Using realistic and defensible aerosol mass concentrations available for transport from the canister interior into an SCC is critical to accurately inform risk analyses and will be considered for parameterization in future experimental studies.

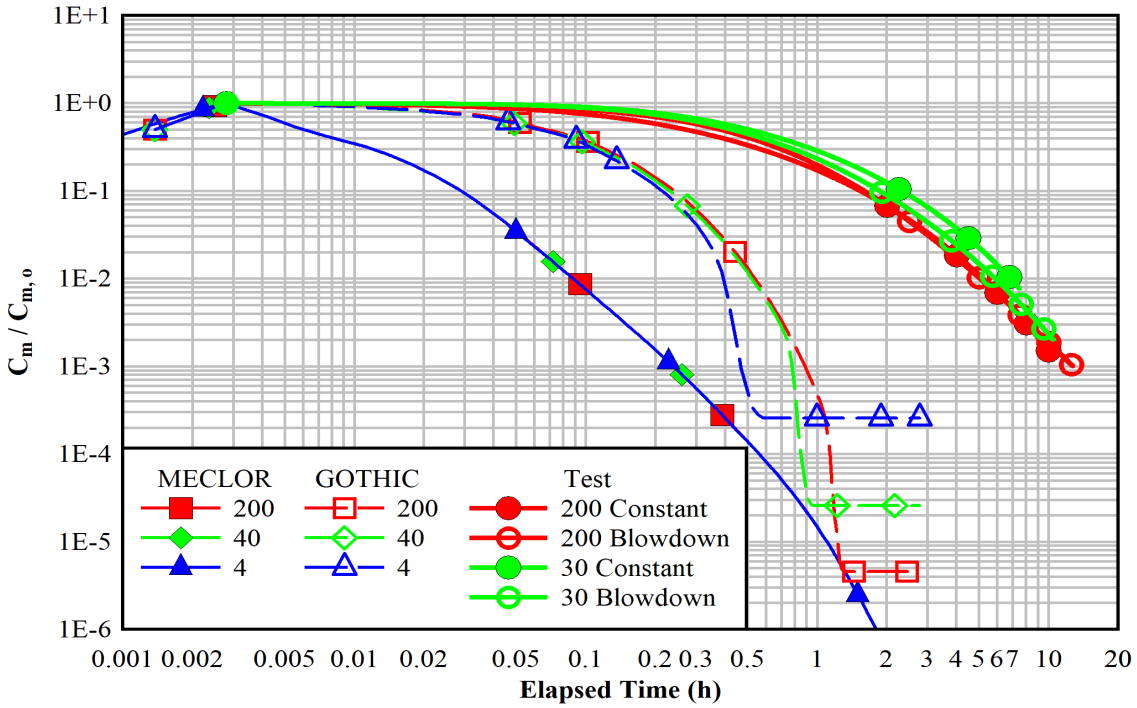

Figure 4.2 Comparison of normalized aerosol mass concentrations from canister models (MELCOR – solid symbols and GOTHIC – open symbols) and experimental measurements (solid and open circles).

5 SUMMARY

Using a microchannel with an initial cross-section of 12.7 mm × 13 μm tapering linearly to 12.7 mm × 25 μm and a flow length of 8.89 mm, a total of thirty aerosol-laden tests were conducted for three nominal initial pressure drops (120 kPa, 420 kPa, and 720 kPa) and two test modes (blowdown and constant pressure). Tests were conducted with both air and helium as the backfill gas. This microchannel represents the typical dimensions of an SCC albeit without any tortuosity and is therefore a relatively conservative simplification of a hypothetical SCC in a dry storage canister for SNF. In the blowdown mode, the supply pressure was allowed to equilibrate to ambient, while in the constant pressure mode, the pressure differential across the channel was held constant. Because aerosol mass transmission largely occurred at the beginning of the tests, there was no discernable difference in the transmission between the blowdown tests and the tests conducted at constant pressure.

The integrated aerosol transmission varied from roughly 0.12 to 0.61 and appears to be inversely proportional to the initial MMD of the test as shown in Figure 5.1. Differences in the procedures for air and helium are being investigated to determine the reason why helium testing tends to have larger initial MMDs. Further testing is needed to better understand the effect of background gas on the results.

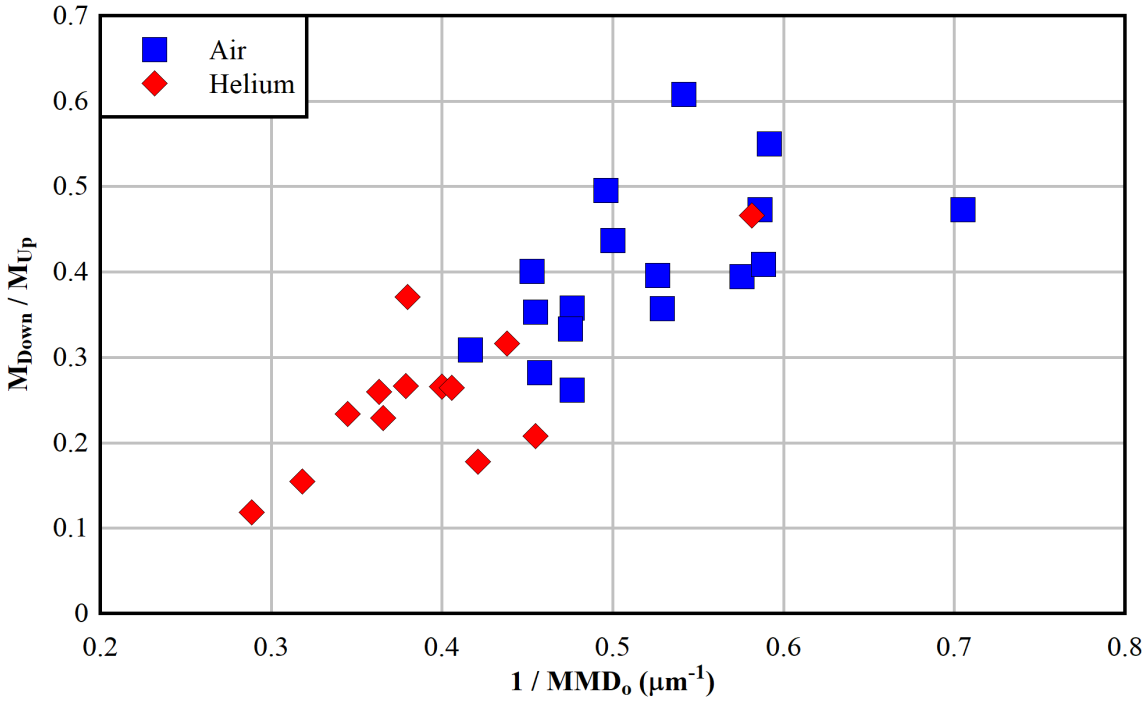

Figure 5.1 Integrated transmission as a function of the inverse of initial mass median diameter.

Initial modeling of the canister interior has indicated that significant aerosol depletion of three orders of magnitude or greater occur within a period of a few hours after a release from the fuel inside the canister. While the specific rates of depletion vary from MELCOR to GOTHIC, this relatively short depletion time is consistently observed across both codes. Additional work is planned to synchronize the initial conditions of the codes in order to facilitate more comparable benchmarking. Studies are also being considered to isolate and model different depletion mechanisms individually and in combination to better understand how a hypothetical fuel release would behave in a storage environment. These modeling results will also inform future transmission testing by providing reference transient aerosol concentrations for canister interiors.

This page is intentionally left blank.

6 REFERENCES

Bixler, N. *et al.*, "State-of-the-Art Reactor Consequence Analyses Project, Volume 1: Peach Bottom Integrated Analysis," US NRC, NUREG/CR-7110 Vol. 1, Rev. 1, May 2013.

Casella, A., S.K. Loyalka, and B.D. Hanson, "Plugging Effects on Depressurization Time in Dry Storage Containers with Pinhole Breaches," **Trans. American Nucl. Soc.**, ***95***, 209-210, Washington, D.C., June (2006).

Casella, A., S.K. Loyalka, and B.D. Hanson, "Pinhole Breaches in Spent Fuel Containers: Improvements to Conservative Models of Aerosol Release and Plugging," **Trans. American Nucl. Soc.**, ***97***, 439-440, Washington, D.C., November (2007).

Chatzidakis, S., and Y. Sasikumar, "Progress Report on Model Development for the Transport of Aerosol through Microchannels," ORNL/SPR-2020/1599, Oak Ridge National Laboratory, Oak Ridge, Tennessee, April (2021).

Durbin, S.D., E.R. Lindgren and R.J.M. Pulido, "Measurement of Particulate Retention in Microchannel Flows", SAND2018-10522R, Sandia National Laboratories, Albuquerque, New Mexico, September (2018).

Durbin, S.G., E.R. Lindgren, and A.G. Perales, "Estimation of Respirable Aerosol Release Fractions through Stress Corrosion Crack-Like Geometries," SAND2020-9014R, M2SF-20SN010207016, Sandia National Laboratories, Albuquerque, New Mexico, August (2020).

EPRI, "Flaw Growth and Flaw Tolerance Assessment for Dry Cask Storage Canisters," EPRI 3002002785 Electric Power Research Institute, Palo Alto, CA, October (2014).

EPRI., "Dry Cask Storage Welded Stainless Steel Canister Breach Consequence Analysis Scoping Study," EPRI 3002008192, Electric Power Research Institute, Palo Alto, CA, November (2017).

GOTHIC, "Thermal Hydraulic Analysis Package, Technical Manual," (2018).

Hanson, B.D., R.C. Daniel, A.M. Casella, R.S. Wittman, W. Wu (BSC), P.J. MacFarlan, and R.W. Shimskey, "Fuel-In-Air FY07 Summary Report," PNNL-17275, Pacific Northwest National Laboratory, Richland, Washington, September (2008).

Humphries L.L., *et al.*, "MELCOR Computer Code Manuals, Vol. 1: Primer and Users' Guide Version 2.2.11932," SAND2018-13559 O, November 2018.

Lanza, M., Casella, A., Elsawi, M., Carstens, N., & Springfels, D., "Thermal Hydraulic Modeling of a Dry Cask and Microchannel," Pacific Northwest National Laboratory Report, PNNL-29225, (2019).

Lanza, M., M. Leimon, M. Elsawi and A. Casella., "GOTHIC Aerosol Source Depletion Studies," PNNL-31176, M3SF-21PN 010207042, Pacific Northwest National Laboratory, Richland, Washington, April (2021).

Lewis, S., "Solid Particle Penetration into Enclosures", J. Hazardous Materials, *43,* 195-216, (1995).

Liu, D-L.and W.W. Nazaroff, "Modeling Pollutant Penetration Across Building Envelopes," **Atmos. Environm**., ***35***, 4451-4462, (2001).

Liu, D-L. and W.W. Nazaroff, "Particle Penetration Through Building Cracks," **Aerosol Science and Technology**, ***37***, 565-573, (2003).

Meyer, R.M., S. Suffield, E.H. Hirt, J.D. Suter, J.P. Lareau, J.W. Zhuge, A. Qiao, T.L. Moran, and P. Ramuhalli, "Nondestructive Examination Guidance for Dry Storage Casks," PNNL-24412 Rev. 1, Pacific Northwest National Laboratory, Richland, Washington, September (2016).

Mosley, R.B., D.J. Greenwell, L.E. Sparks, Z. Guo, W.G. Tucker, R. Fortmann, C. Whitfield, "Penetration of Ambient Fine Particles into the Indoor Environment," **Aerosol Science and Technology**, ***34***, 127-136, (2001).

Nakos, J.T., "Uncertainty Analysis of Thermocouple Measurements Used in Normal and Abnormal Thermal Environment Experiments at Sandia's Radiant Heat Facility and Lurance Canyon Burn Site," SAND2004-1023, Sandia National Laboratories, Albuquerque, NM, April 2004.

NRC, "Spent Fuel Transportation Risk Assessment," United States Nuclear Regulatory Commission, NUREG-2125, May (2012).

Palas GmbH, "RBG 1000 Particle Generator Manual," Karlsruhe, Germany, (2002).

Phillips, J. and F. Gelbard., "Interim Report on Aerosol Deposition Inside a Spent Fuel Transportation and Storage Canister," SAND2021-5202R, M3SF-21SN010207072, Sandia National Laboratories, Albuquerque, New Mexico, April (2021).

Powers, D.A., "Aerosol Penetration of Leak Pathways – An Examination of the Available Data and Models," SAND2009-1701, Sandia National Laboratories, Albuquerque, NM, April (2009).

Sanders, T.L., K.D. Seager, Y.R. Rashid, P.R. Barrett, A.P. Malinauskas, R.E. Einziger, H. Jordan, T.A. Duffey, S.H. Sutherland, and P.C. Reardon "A Method for Determining the Spent-Fuel Contribution to Transport Cask Containment Requirements," SAND90-2406, Sandia National Laboratories, Albuquerque, NM, November (1992).

Schindelholz, E., C. Bryan, and C. Alexander, "FY17 Status Report: Research on Stress Corrosion Cracking of SNF Interim Storage Canisters," SAND2017-10338R, Sandia National Laboratories, Albuquerque, NM, August (2017).

APPENDIX A TRANSIENT AEROSOL MASS CONCENTRATIONS

Upstream and downstream temporal mass concentrations are presented in this appendix for all tests. The raw data from the Welas 2200 aerosol sensors are plotted alongside the fourth-order log-log polynomial fits to the raw data. For each plot, the start time for the polynomial fits was chosen to be between 0 and 0.1 hours in order to capture as much of the raw data trends as possible. The end time for the polynomial fits was chosen by a logical statement defined by when the downstream test section Welas sensor detects 25 or less particles, at which point the analyzed particle number measurements no longer hold statistical significance.

The tests presented in this appendix are defined by the test date, either the pressure difference between the upstream and downstream test sections at the start of the test for blowdown tests (ΔP_o) or the maintained pressure difference for the constant pressure tests (ΔP), the background gas (air or helium), the test type (blowdown or constant pressure), and the initial upstream concentration at STP ($C_{m,Up,STP,o}$). The measured initial upstream concentration ($C_{m,Up,o}$) is also provided.

A.1 Air Tests

A.1.1 120 kPa Air

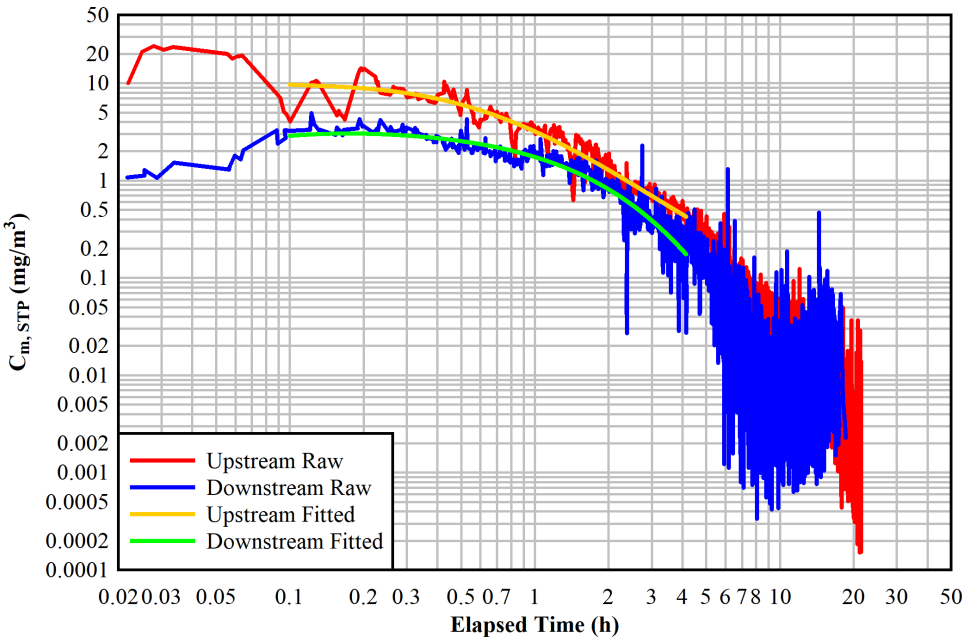

Figure A.1 Raw and curve-fit aerosol mass concentrations for the test on 06/11/2021 with air blowdown from ΔP_o = 119 kPa and an initial upstream concentration of $C_{m,Up,STP,o}$ = 9.26 mg/m^3 ($C_{m,Up,o}$ = 18.7 mg/m^3).

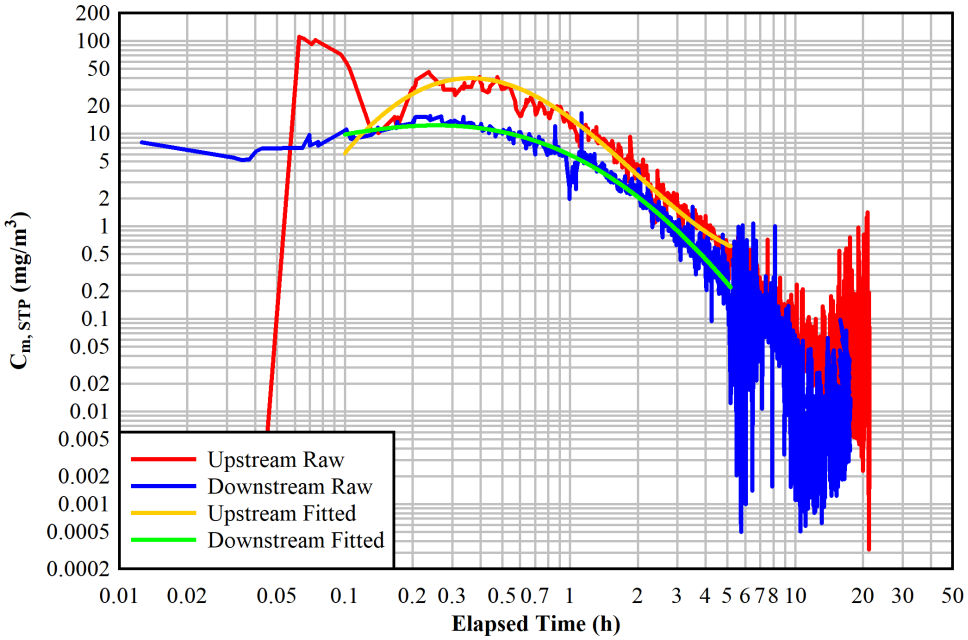

Figure A.2 Raw and curve-fit aerosol mass concentrations for the test on 05/06/2021 with air blowdown from ΔP_o = 120 kPa and an initial upstream concentration of $C_{m, Up, STP, o}$ = 16.6 mg/m^3 ($C_{m, Up, o}$ = 33.6 mg/m^3).

A.1.2 420 kPa Air

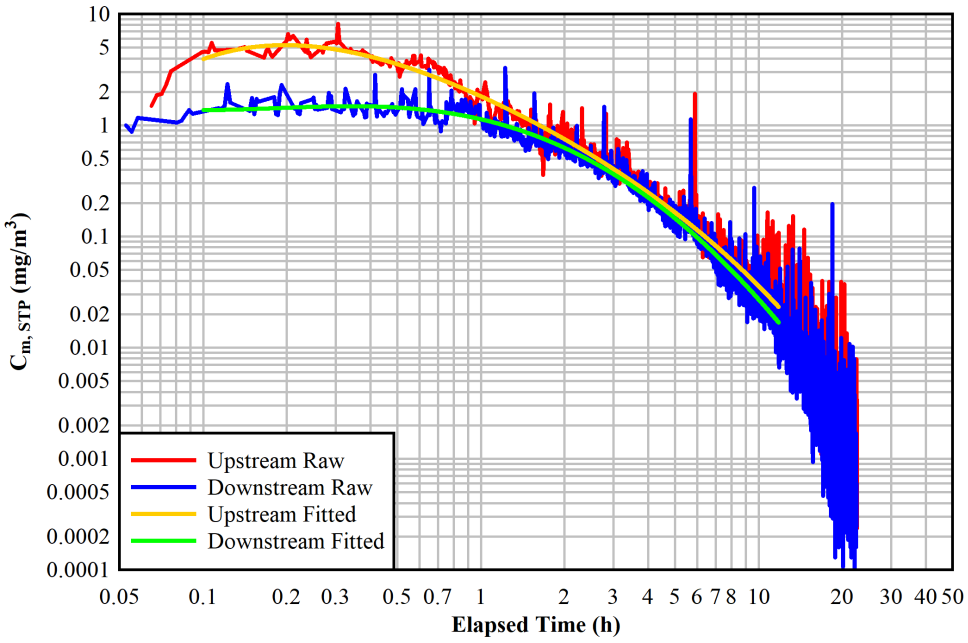

Figure A.3 Raw and curve-fit aerosol mass concentrations for the test on 06/13/2021 with air blowdown from ΔP_o = 415 kPa and an initial upstream concentration of $C_{m, Up, STP, o}$ = 4.90 mg/m^3 ($C_{m, Up, o}$ = 24.5 mg/m^3).

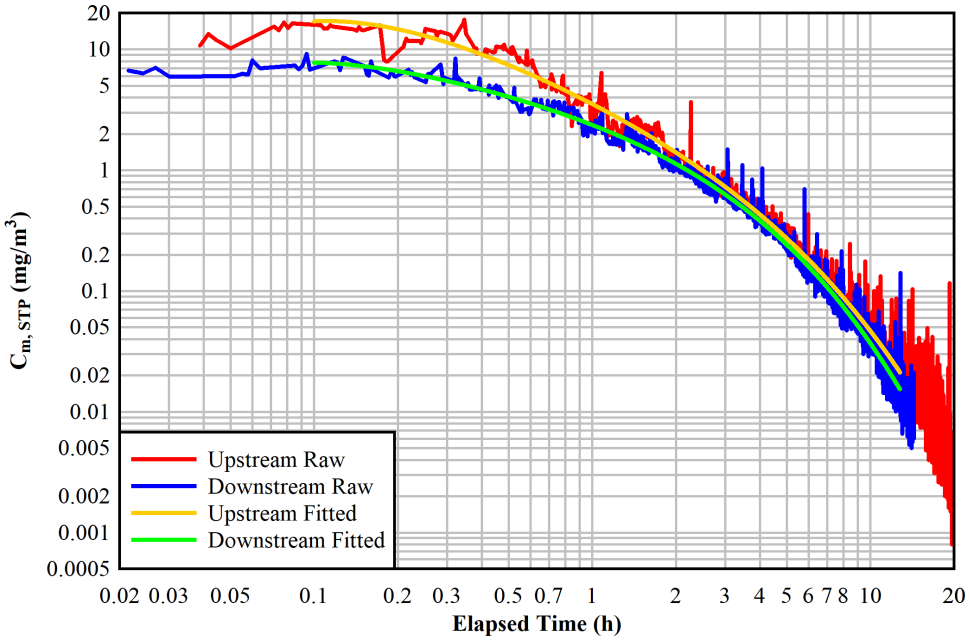

Figure A.4 Raw and curve-fit aerosol mass concentrations for the test on 06/12/2021 with air blowdown from ΔP_o = 418 kPa and an initial upstream concentration of $C_{m, Up, STP, o}$ = 16.3 mg/m^3 ($C_{m, Up, o}$ = 81.1 mg/m^3).

A.1.3 720 kPa Air

A.1.3.1 720 kPa Air Blowdown

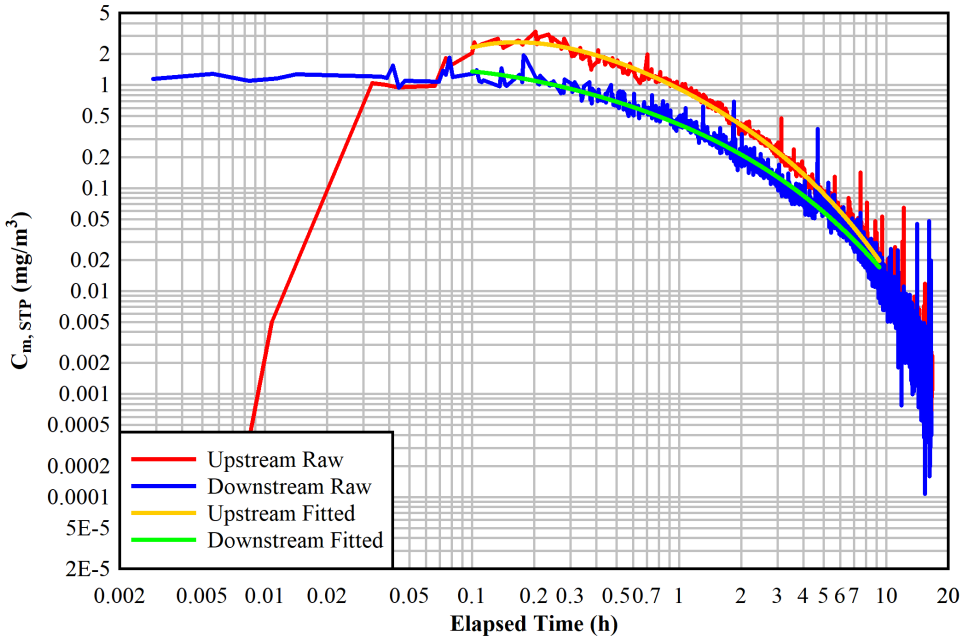

Figure A.5 Raw and curve-fit aerosol mass concentrations for the test on 04/29/2021 with air blowdown from ΔP_o = 716 kPa and an initial upstream concentration of $C_{m, Up, STP, o}$ = 2.55 mg/m^3 ($C_{m, Up, o}$ = 20.1 mg/m^3).

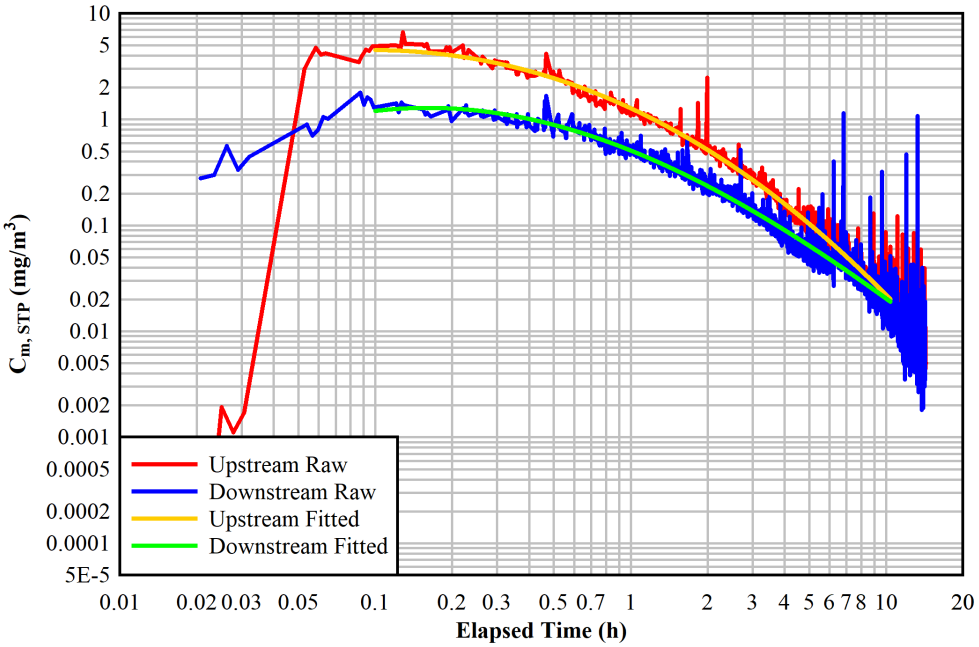

Figure A.6 Raw and curve-fit aerosol mass concentrations for the test on 06/02/2021 with air blowdown from ΔP_o = 717 kPa and an initial upstream concentration of $C_{m, Up, STP, o}$ = 4.30 mg/m^3 ($C_{m, Up, o}$ = 34.2 mg/m^3).

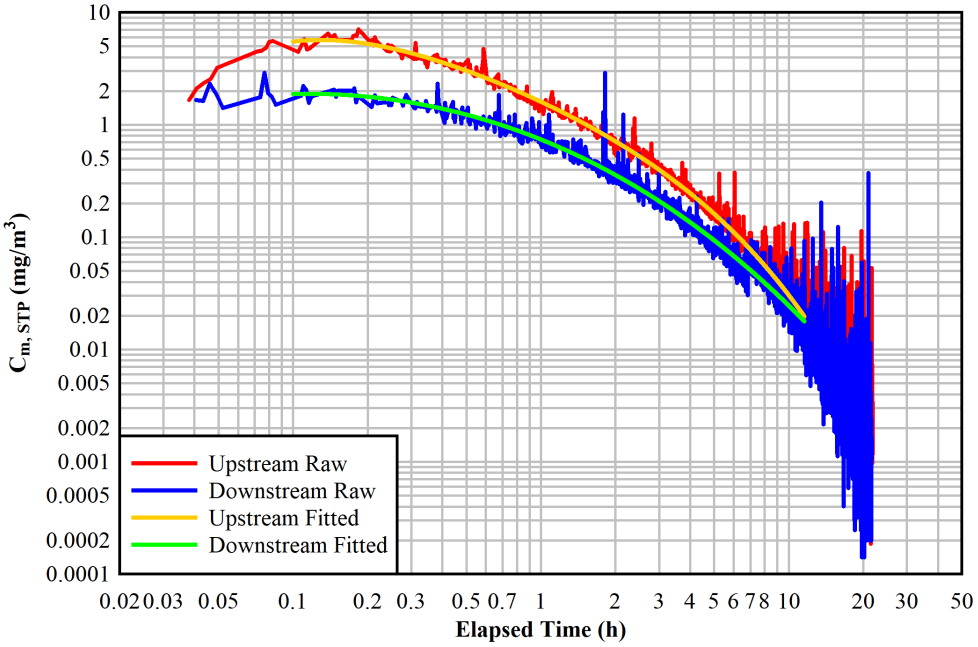

Figure A.7 Raw and curve-fit aerosol mass concentrations for the test on 06/03/2021 with air blowdown from ΔP_o = 723 kPa and an initial upstream concentration of $C_{m, Up, STP, o}$ = 5.60 mg/m^3 ($C_{m, Up, o}$ = 44.2 mg/m^3).

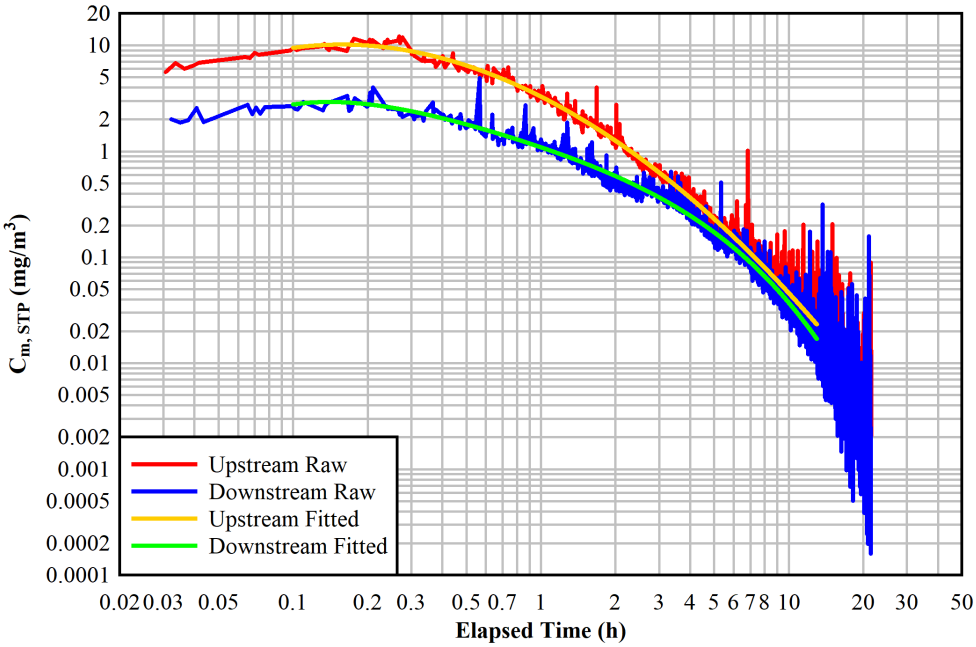

Figure A.8 Raw and curve-fit aerosol mass concentrations for the test on 06/08/2021 with air blowdown from ΔP_o = 717 kPa and an initial upstream concentration of $C_{m, Up, STP, o}$ = 10.0 mg/m^3 ($C_{m, Up, o}$ = 79.1 mg/m^3).

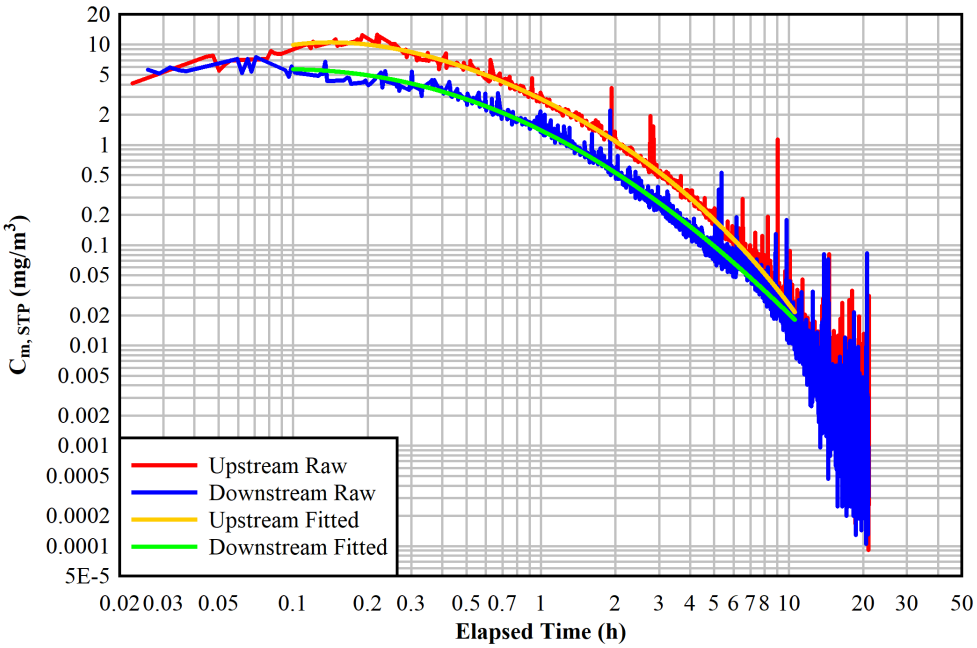

Figure A.9 Raw and curve-fit aerosol mass concentrations for the test on 05/04/2021 with air blowdown from ΔP_o = 717 kPa and an initial upstream concentration of $C_{m, Up, STP, o}$ = 10.4 mg/m^3 ($C_{m, Up, o}$ = 81.4 mg/m^3).

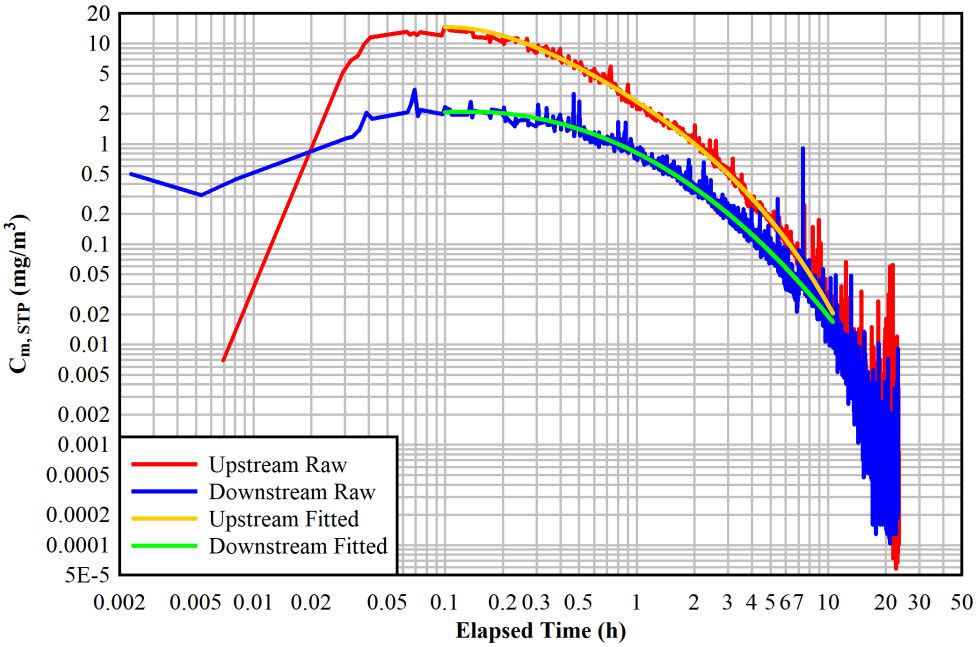

Figure A.10 Raw and curve-fit aerosol mass concentrations for the test on 04/28/2021 with air blowdown from ΔP_o = 717 kPa and an initial upstream concentration of $C_{m, Up, STP, o}$ = 13.6 mg/m^3 ($C_{m, Up, o}$ = 108 mg/m^3).

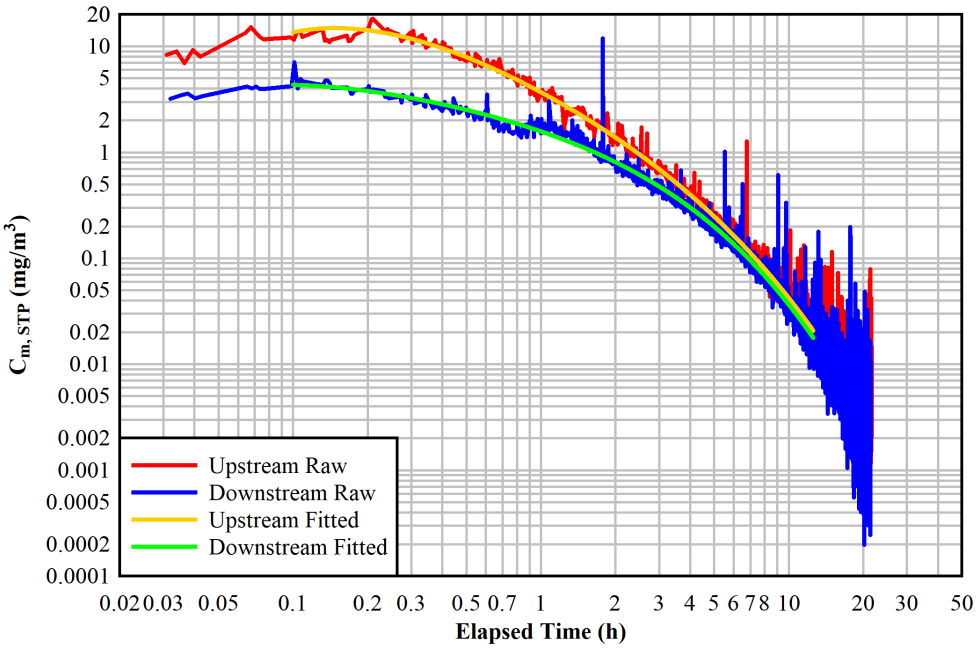

Figure A.11 Raw and curve-fit aerosol mass concentrations for the test on 06/01/2021 with air blowdown from ΔP_o = 717 kPa and an initial upstream concentration of $C_{m, Up, STP, o}$ = 14.6 mg/m^3 ($C_{m, Up, o}$ = 115 mg/m^3).

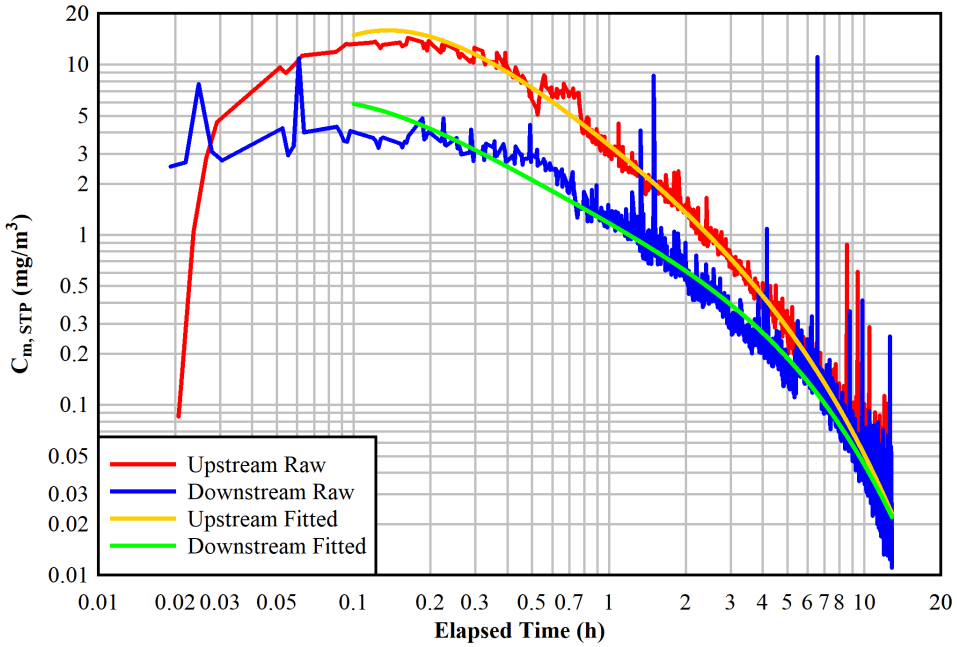

Figure A.12 Raw and curve-fit aerosol mass concentrations for the test on 06/09/2021 with air blowdown from ΔP_o = 717 kPa and an initial upstream concentration of $C_{m, Up, STP, o}$ = 15.5 mg/m^3 ($C_{m, Up, o}$ = 123 mg/m^3).

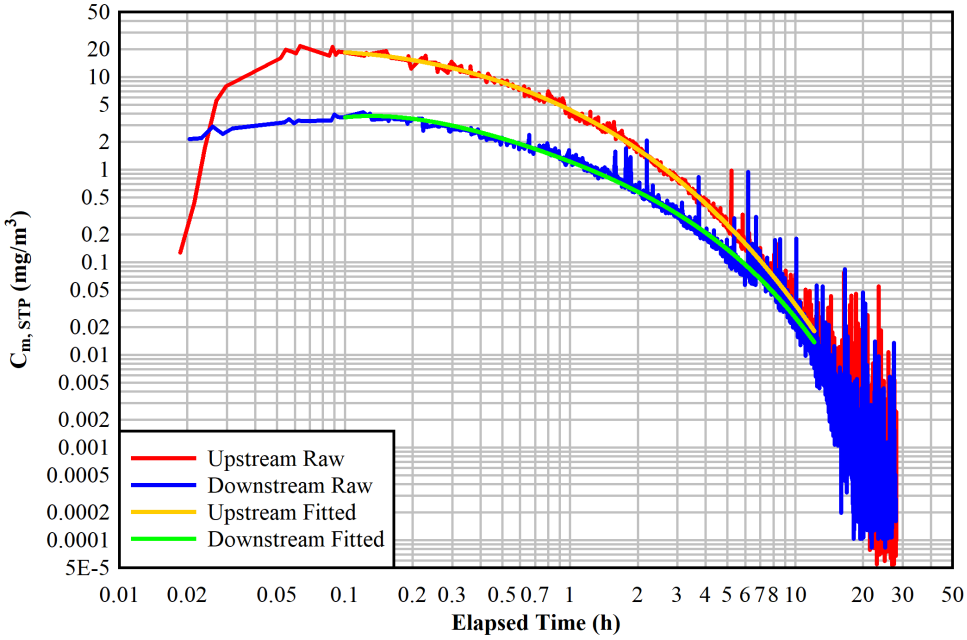

Figure A.13 Raw and curve-fit aerosol mass concentrations for the test on 05/03/2021 with air blowdown from ΔP_o = 717 kPa and an initial upstream concentration of $C_{m, Up, STP, o}$ = 16.8 mg/m^3 ($C_{m, Up, o}$ = 134 mg/m^3).

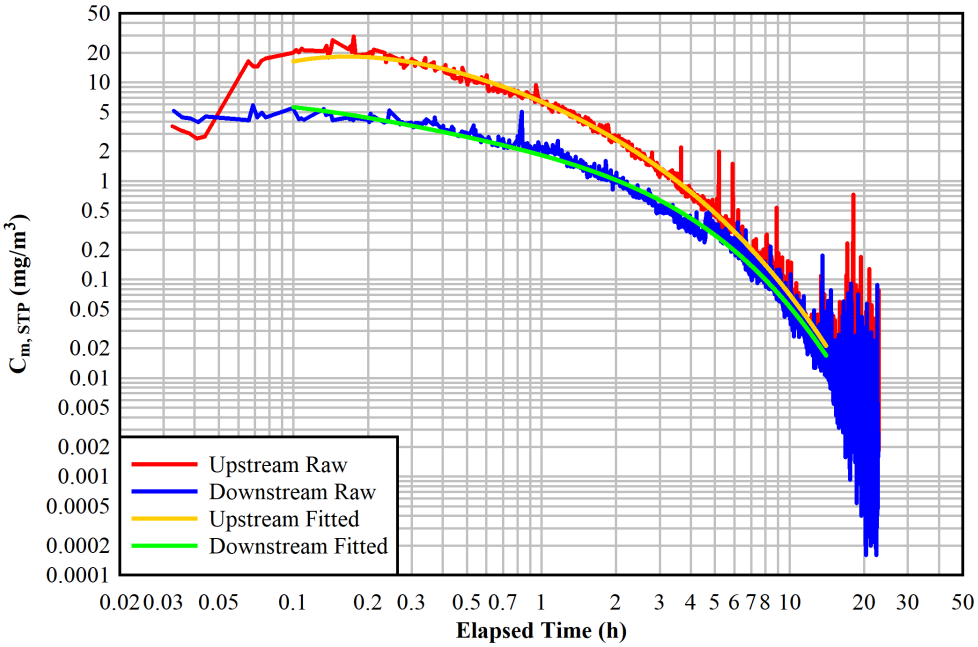

Figure A.14 Raw and curve-fit aerosol mass concentrations for the test on 05/26/2021 with air blowdown from ΔP_o = 717 kPa and an initial upstream concentration of $C_{m, Up, STP, o}$ = 17.9 mg/m^3 ($C_{m, Up, o}$ = 141 mg/m^3).

A.1.3.2 720 kPa Air Constant Pressure

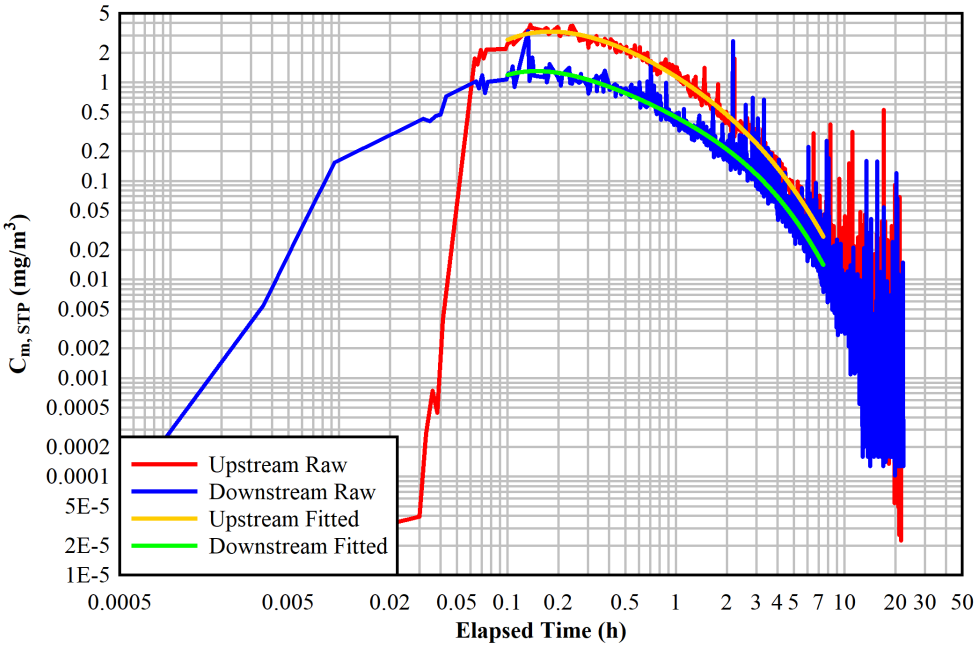

Figure A.15 Raw and curve-fit aerosol mass concentrations for the test on 06/10/2021 with air at constant pressure (ΔP = 717 kPa) and an initial upstream concentration of $C_{m, Up, STP, o}$ = 3.10 mg/m^3 ($C_{m, Up, o}$ = 25.2 mg/m^3).

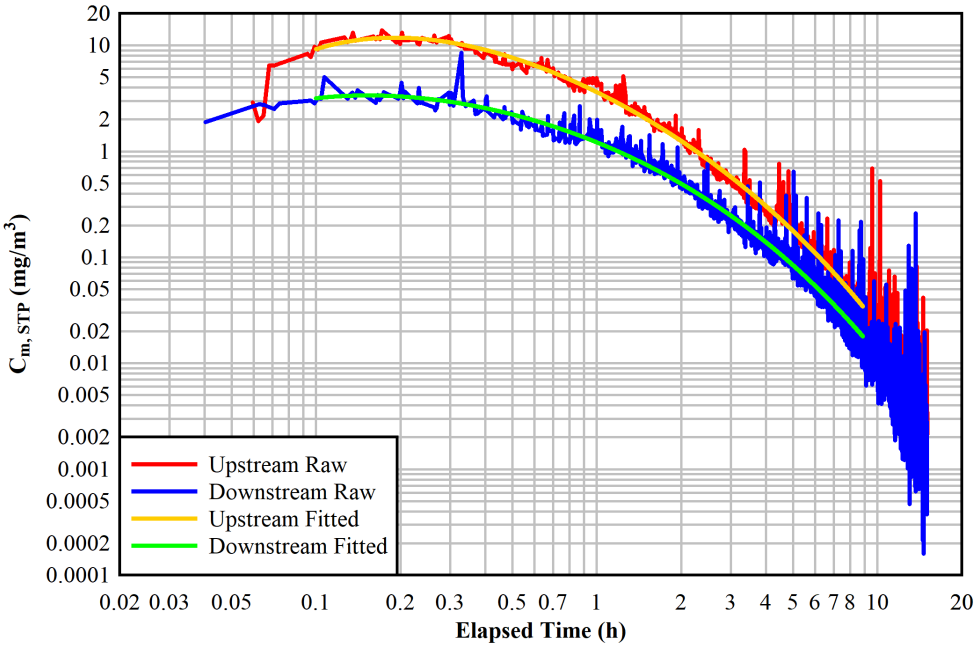

Figure A.16 Raw and curve-fit aerosol mass concentrations for the test on 06/07/2021 with air at constant pressure (ΔP = 714 kPa) and an initial upstream concentration of $C_{m, Up, STP, o}$ = 11.1 mg/m^3 ($C_{m, Up, o}$ = 89.3 mg/m^3).

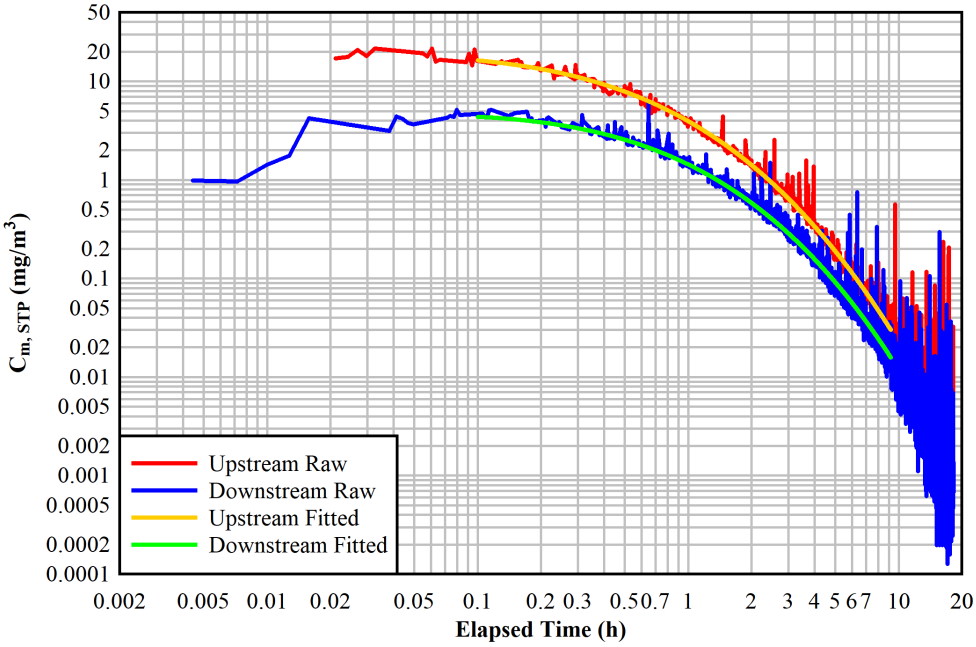

Figure A.17 Raw and curve-fit aerosol mass concentrations for the test on 06/04/2021 with air at constant pressure (ΔP = 716 kPa) and an initial upstream concentration of $C_{m, Up, STP, o}$ = 14.8 mg/m^3 ($C_{m, Up, o}$ = 119 mg/m^3).

A.2 Helium Tests

A.2.1 420 kPa Helium

A.2.1.1 420 kPa Helium Blowdown

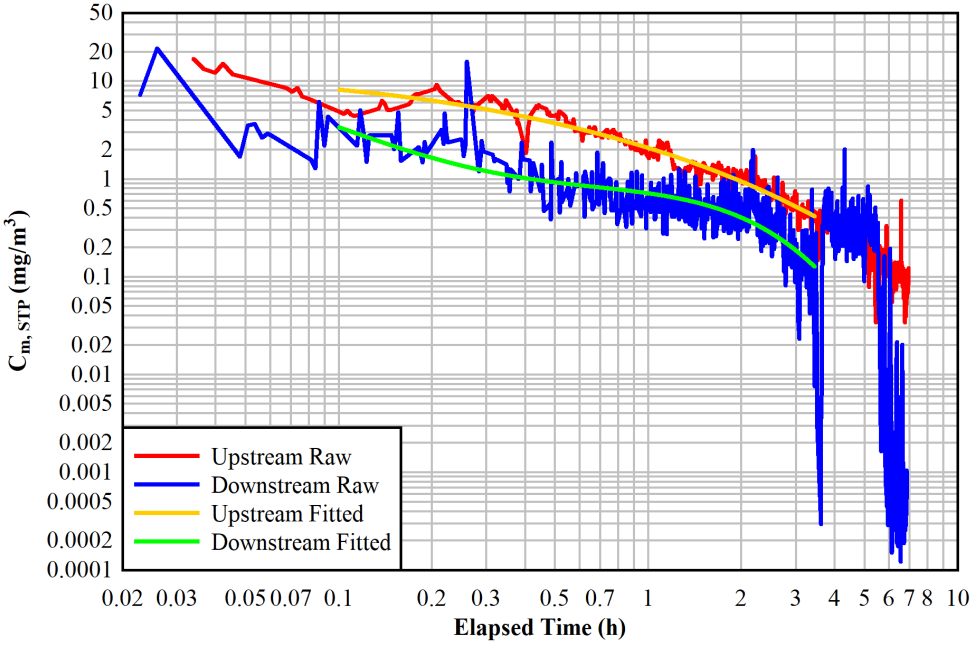

Figure A.18 Raw and curve-fit aerosol mass concentrations for the test on 06/25/2021 with helium blowdown from ΔP_o = 418 kPa and an initial upstream concentration of $C_{m, Up, STP, o}$ = 7.20 mg/m^3 ($C_{m, Up, o}$ = 35.8 mg/m^3).

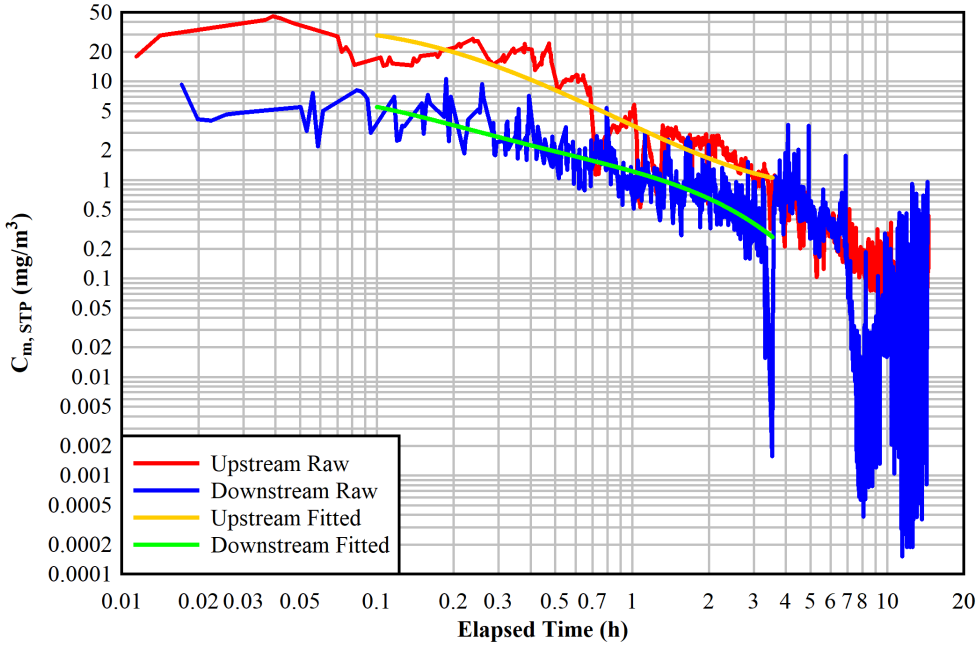

Figure A.19 Raw and curve-fit aerosol mass concentrations for the test on 06/24/2021 with helium blowdown from ΔP_o = 417 kPa and an initial upstream concentration of $C_{m, Up, STP, o}$ = 24.3 mg/m^3 ($C_{m, Up, o}$ = 121 mg/m^3).

A.2.1.2 420 kPa Helium Constant Pressure

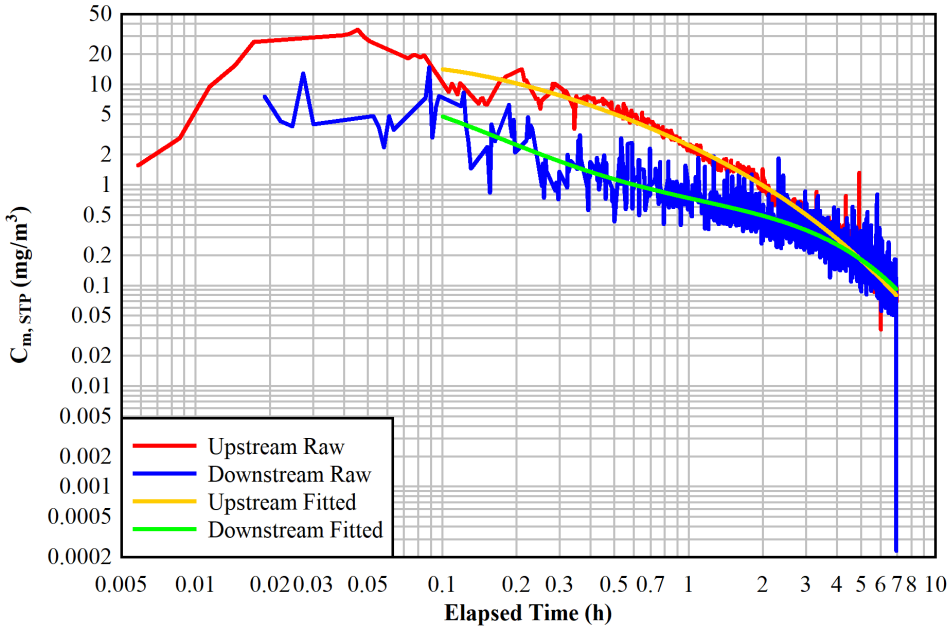

Figure A.20 Raw and curve-fit aerosol mass concentrations for the test on 06/30/2021 with helium at constant pressure (ΔP = 417 kPa) and an initial upstream concentration of $C_{m, Up, STP, o}$ = 12.1 mg/m^3 ($C_{m, Up, o}$ = 61.1 mg/m^3).

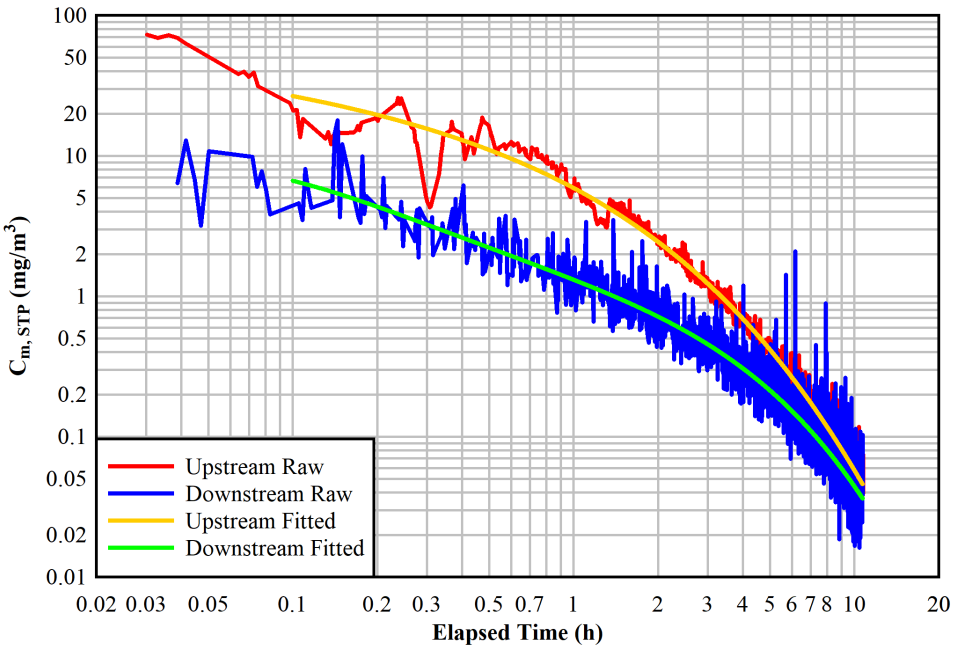

Figure A.21 Raw and curve-fit aerosol mass concentrations for the test on 06/29/2021 with helium at constant pressure (ΔP = 418 kPa) and an initial upstream concentration of $C_{m, Up, STP, o}$ = 22.7 mg/m^3 ($C_{m, Up, o}$ = 114 mg/m^3).

A.2.2 720 kPa Helium

A.2.2.1 720 kPa Helium Blowdown

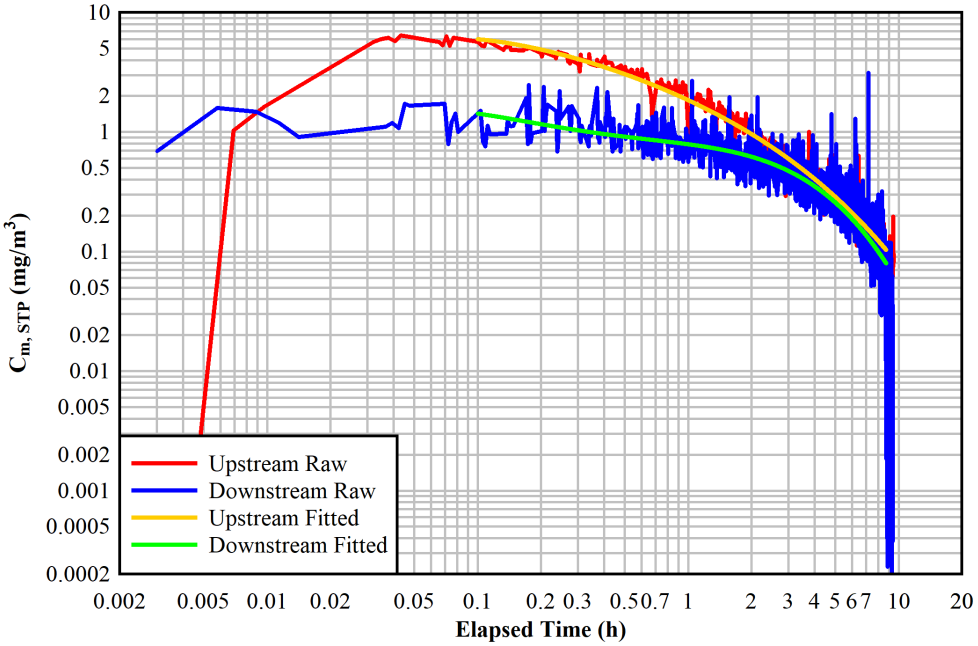

Figure A.22 Raw and curve-fit aerosol mass concentrations for the test on 07/13/2021 with helium blowdown from ΔP_o = 716 kPa and an initial upstream concentration of $C_{m, Up, STP, o}$ = 5.43 mg/m^3 ($C_{m, Up, o}$ = 43.0 mg/m^3).

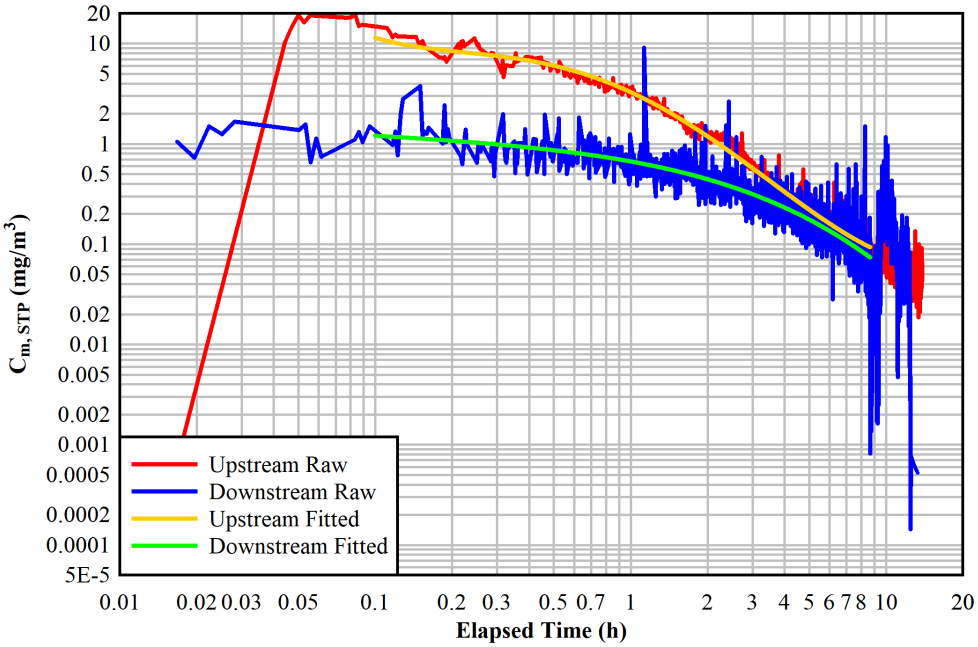

Figure A.23 Raw and curve-fit aerosol mass concentrations for the test on 06/28/2021 with helium blowdown from ΔP_o = 717 kPa and an initial upstream concentration of $C_{m, Up, STP, o}$ = 9.40 mg/m^3 ($C_{m, Up, o}$ = 74.8 mg/m^3).

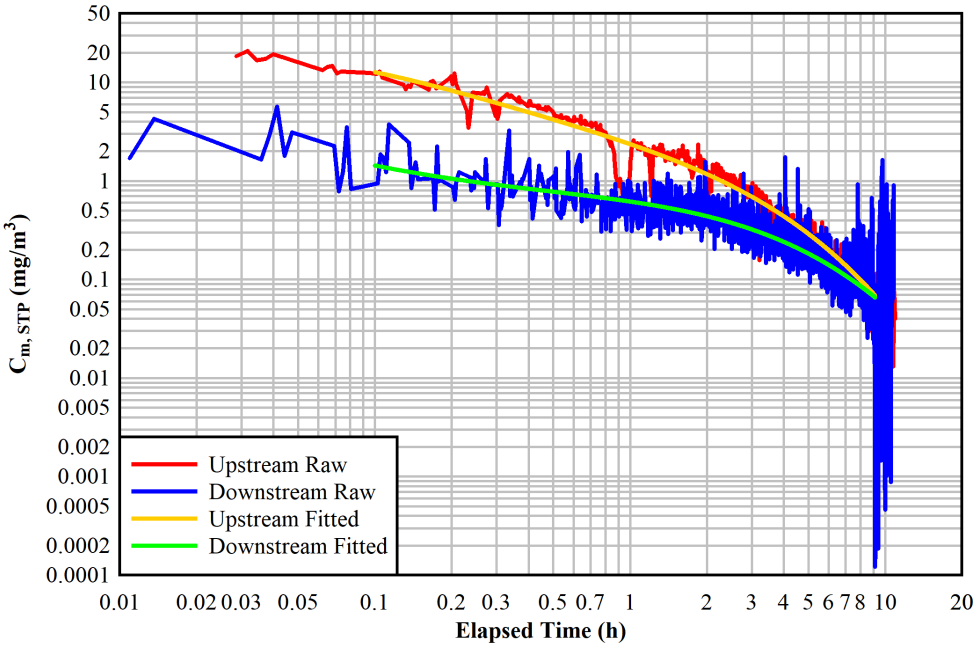

Figure A.24 Raw and curve-fit aerosol mass concentrations for the test on 06/20/2021 with helium blowdown from ΔP_o = 739 kPa and an initial upstream concentration of $C_{m, Up, STP, o}$ = 10.1 mg/m^3 ($C_{m, Up, o}$ = 82.5 mg/m^3).

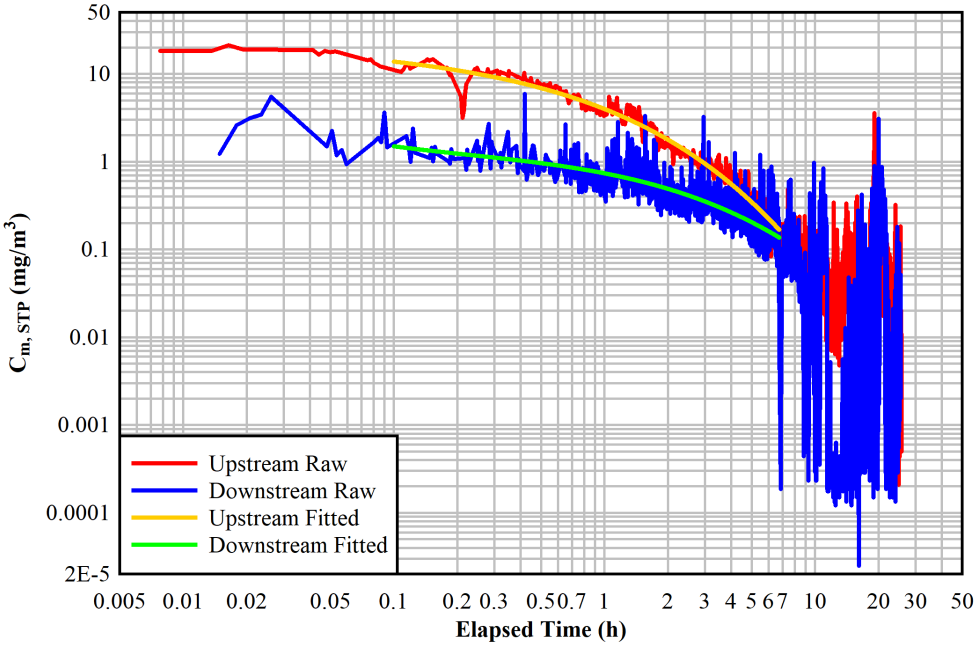

Figure A.25 Raw and curve-fit aerosol mass concentrations for the test on 06/17/2021 with helium blowdown from ΔP_o = 713 kPa and an initial upstream concentration of $C_{m, Up, STP, o}$ = 11.0 mg/m^3 ($C_{m, Up, o}$ = 86.8 mg/m^3).

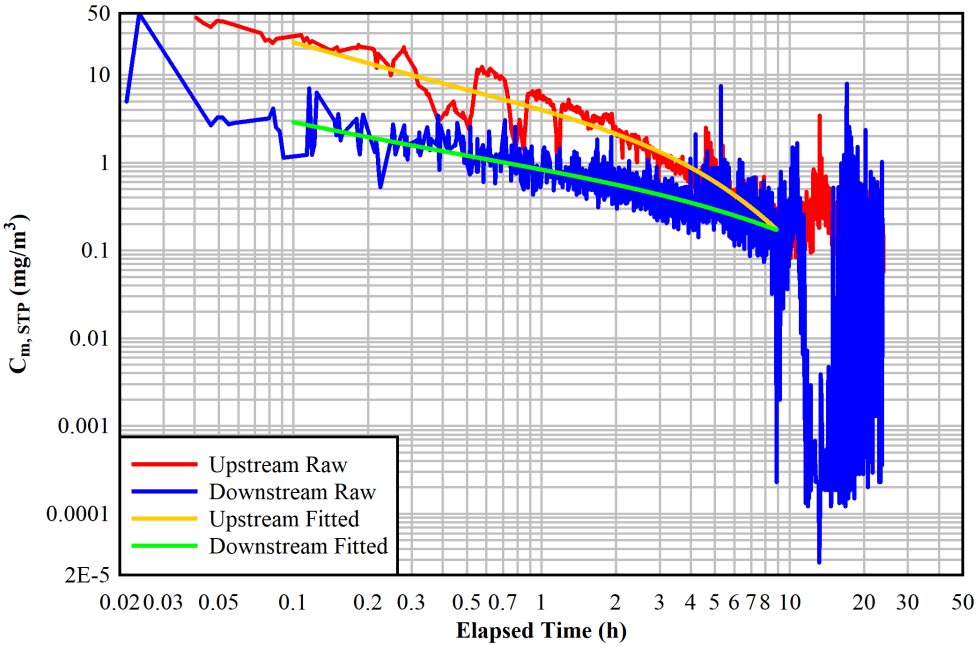

Figure A.26 Raw and curve-fit aerosol mass concentrations for the test on 06/21/2021 with helium blowdown from ΔP_o = 716 kPa and an initial upstream concentration of $C_{m, Up, STP, o}$ = 17.5 mg/m^3 ($C_{m, Up, o}$ = 139 mg/m^3).

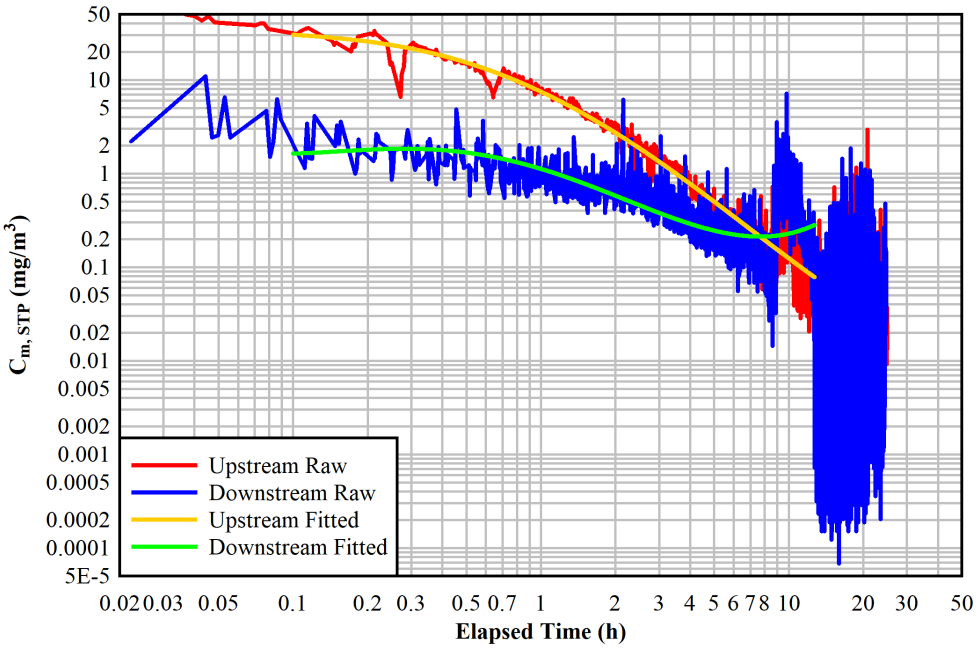

Figure A.27 Raw and curve-fit aerosol mass concentrations for the test on 06/19/2021 with helium blowdown from ΔP_o = 719 kPa and an initial upstream concentration of $C_{m, Up, STP, o}$ = 28.0 mg/m^3 ($C_{m, Up, o}$ = 224 mg/m^3).

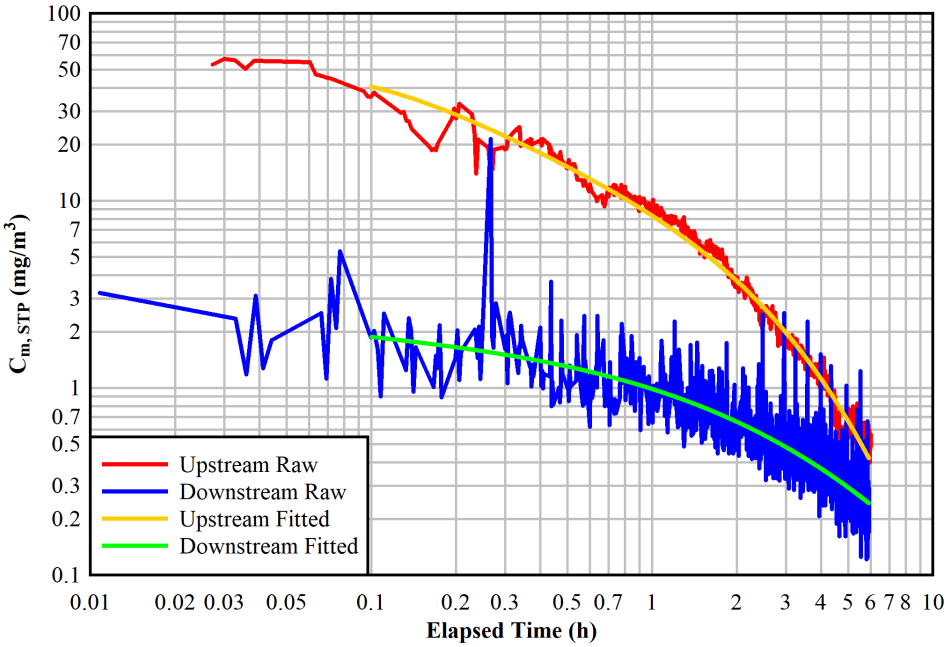

Figure A.28 Raw and curve-fit aerosol mass concentrations for the test on 06/29/2021 with helium blowdown from ΔP_o = 715 kPa and an initial upstream concentration of $C_{m, Up, STP, o}$ = 34.2 mg/m^3 ($C_{m, Up, o}$ = 273 mg/m^3).

A.2.2.2 720 kPa Helium Constant Pressure

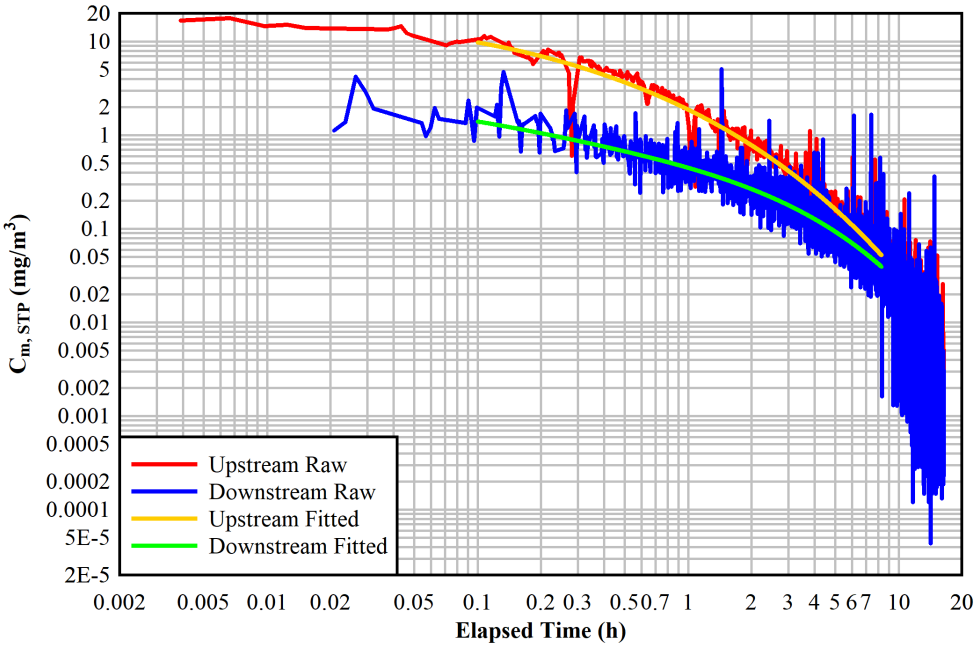

Figure A.29 Raw and curve-fit aerosol mass concentrations for the test on 06/18/2021 with helium at constant pressure (ΔP = 716 kPa) and an initial upstream concentration of $C_{m, Up, STP, o}$ = 8.26 mg/m^3 ($C_{m, Up, o}$ = 66.4 mg/m^3).

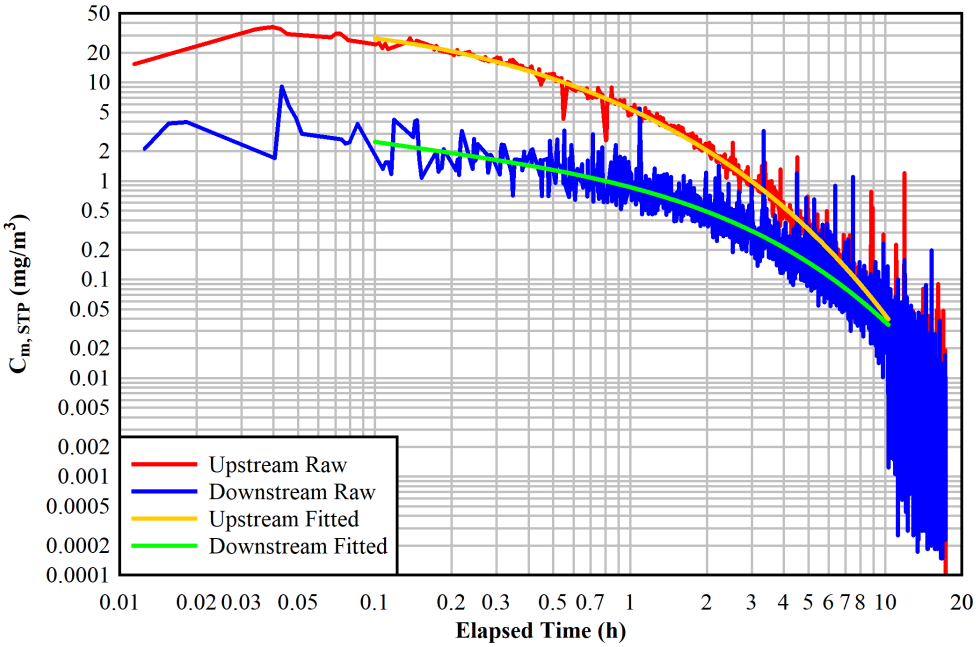

Figure A.30 Raw and curve-fit aerosol mass concentrations for the test on 06/16/2021 with helium at constant pressure (ΔP = 720 kPa) and an initial upstream concentration of $C_{m, Up, STP, o}$ = 24.0 mg/m^3 ($C_{m, Up, o}$ = 193 mg/m^3).

Sandia National Laboratories